Development and validation of a personalizable model of the hepatic arterial tree and particle transport

by

Nathan R. Crookston

A dissertation submitted to Johns Hopkins University in conformity with the requirements for the degree of Doctor of Philosophy.

Baltimore, Maryland

April, 2019

Abstract

Liver cancers are increasingly common and require improved treatment methods. Radioembolization inhibits tumor growth by inserting small spheres into the hepatic artery that are carried into smaller vessels near tumors, where they deposit radiation. Predicting toxicity for this treatment is challenging due to the microanatomical liver structure and the tendency of microspheres to cluster when trapped.

This work describes and validates a novel method to generate personalized hepatic arterial tree models and simulate realistic glass microsphere distributions. It describes methods to generate realistic arterial trees using physically constrained macrocell growth models that can incorporate measurable parameters such as initial and terminal vessel diameters and blood pressure. It also describes models of microsphere infusion that simulate different embolic effects and trapping behavior. Microsphere cluster-size histograms and images at PET resolution were simulated for several infusion methods in a hepatic arterial tree model generated from liver and proper hepatic artery segmentations taken from the XCAT phantom.

To verify the distributions created through microsphere infusion simulation, a characterization of the three-dimensional clustering of glass microspheres in tissue was necessary. However, traditional methods to find microsphere locations requires creating thin slices of treated tissue that are stained and examined microscopically, which is a very time-consuming process. This thesis describes how to use micro-CT and image processing to detect glass microspheres in whole tissue samples. The detection method was verified by processing phantoms composed of glass microspheres embedded in agar that could also be imaged microscopically to determine true microsphere locations. Using this, $>93\%$ of microspheres in the phantom were correctly detected and the percentage of erroneously detected microspheres was $<5\%$. The mean absolute error between the true and estimated dose maps was 4.2%.

The detection method was then applied to a treated porcine liver sample to characterize microsphere clustering behavior in normal liver tissue. A histogram of these cluster sizes was compared with histograms simulated using the tree and transport models. The most realistic clustering behavior was produced by having microspheres trap in vessels when their diameters exceeded the vessel diameters, and when embolic effects did not affect later microsphere traversal.

ABSTRACT

Primary Reader and Advisor: Eric C. Frey

Secondary Reader: Gerard G. L. Meyer

Acknowledgments

I have been very fortunate to have Dr. Eric Frey as my advisor during my time at Johns Hopkins University. He encouraged me to pursue my research as it developed in unexpected ways, provided invaluable advice and feedback, and generally demonstrated exemplary professional mentorship. Like most would-be graduate students, I didn't really understand what I was signing up for when I went back to school, but I am confident that I couldn't have had a better advisor.

I am also grateful to Drs. Ken Taguchi, Abhinav Kumar Jha, Michael Ghaly, Yong Du, Andrew Rittenbach, and Ben Tsui for their friendship and guidance. Each of them provided encouragement and inspiration during my studies that helped me overcome difficult research challenges.

I am thankful to Debbie Race, Michele Ingram, and Martin Stumpf for always being willing to help when I was trying to understand graduation requirements, had my building access revoked, or needed more disk space on the cluster for the umpteenth time.

ACKNOWLEDGMENTS

I am indebted to Drs. Alex Pasciak and Godwin Abiola for offering me the opportunity to work on their project. It was exactly what I wanted to do at exactly the right time. This work would be significantly different (and in my mind, much less satisfying) if they hadn't reached out to me when they did.

To my friend and fellow student, Gary Li, thanks for making work fun, and for suffering through my journal club presentations without complaint.

Finally, thanks to my wife and my parents for always encouraging me to reach for my goals, and thanks to my four children for always encouraging me to abandon my goals and come play with them. Looking at it philosophically, my life has been best when I do some of each.

Dedication

To my wife, Ashley, my children, Andrew, Anne, Kate, and Emma, my parents, Allen and Sherry, and my Savior.

Contents

List of Figures

Acronyms

CT computed tomography. 5

DVK dose-voxel kernel. 73

EBRT external beam radiation therapy. 1, 2, 19, 20, 31, 32

FN false negative. 72, 74, 111

FP false positive. 72–74, 98, 111

FPF false positive fraction. 73, 80, 81, 83, 88, 99, 104, 111

HA hepatic artery. 8, 9, 17, 32

HAT hepatic arterial tree. 3, 11, 95–97, 102, 107

HU Hounsfield units. 62, 77, 79–83

LET linear energy transfer. 14

MAA macroaggregated albumin. 18, 19, 54

MAE mean absolute error. 74, 75, 83, 84, 88, 90

MIP maximum-intensity projection. 71, 78, 86, 89

MTAD maximum tolerable absorbed dose. 6, 19

NBG no-background. 67, 68, 72, 80–82, 87, 89, 98, 99, 104

PHA proper hepatic artery. 33, 36, 37, 39, 44, 46–48, 50

PV portal vein. 8

RE radioembolization. 1, 2, 4–7, 10, 19, 20, 31, 32, 35, 54, 57, 75, 91, 116, 117

TACE trans-arterial chemoembolization. 11, 20

TAE trans-arterial embolization. 20

THA terminal hepatic arteriole. 8, 9, 34, 36–40, 42–53, 102, 107, 112

TP true positive. 72, 73

TPF true positive fraction. 73, 80, 81, 83, 99, 104

VDR vessel diameter ratio. 37–39, 46, 49

WBG with-background. 66–68, 72, 80–83, 87–89

Chapter 1

Introduction

Liver cancer is one of the most fatal and rapidly increasing forms of cancer [1–3], with 400,000 new cases diagnosed each year in the US and an even higher incidence rate in other countries [4, 5]. The liver is also a common site for metastatic cancer growth [6]. Because of this, there is interest in improving patient treatment and outcomes. One form of treatment is radioembolization (RE), a minimally-invasive form of targeted treatment that uses a catheter to deliver radioactive particles within the hepatic arterial tree. Those particles embed in the liver near tumors, reduce blood flow in trapping vessels, and deliver very high radiation doses that damage nearby cells and tissues [7].

The doses absorbed using RE far exceed what is possible using external beam radiation therapy (EBRT) without inducing liver toxicity [8]. Absorbed dose from EBRT is deposited uniformly in tissues the beam passes through, while the clustered distribution of microspheres inserted trans-arterially deposits a very heterogeneous dose [9]. This, together with the higher chance of microspheres trapping near tumors and the unique structure of liver microanatomy, is thought to spare normal liver tissue [10, 11].

The best patient outcomes occur when tumors receive the highest doses [12] and sufficient normal liver tissue remains functional to compensate for tissue that has been damaged by disease or radiation. Treatment plans specify the administered activity, typically based on quantitative imaging of the patient, to achieve these outcomes.

However, predicting the dose to tumors for a particular administered activity is recognized as very challenging [13]. In addition, the toxic dose for tumors is typically more variable than for normal tissue due to the heterogeneity of liver tumor cells. Because of this, it has been argued that delivering the highest safe dose to normal liver tissue will also provide the highest dose to tumor tissues and increase the probability of tumor control [14]. The mechanism by which normal liver tissue survives the high absorbed doses delivered by RE is incompletely understood, which limits the accuracy of predictions of normal tissue toxicity and therefore tumor control.

1.1 Significance

Previous studies have attempted to understand the absorbed dose tolerance of normal liver tissues by modeling the hepatic arterial tree (HAT) and simulating microsphere infusions and trapping [10]. However, the predicted microsphere cluster distributions from those simulations have not been verified *in vivo*, and the structure of the HAT models had some aspects that were physically unrealistic [15]. The ability to model personalized, physically realistic HATs suitable for microsphere infusion simulation could allow different treatment plans to be compared and the resulting small-scale dose distributions to be analyzed.

Better treatment planning methods could be developed if the non-uniform doses due to microsphere clustering and the effects on liver tissue were better understood.

In order to verify that the clusters produced using a physically realistic model of the HAT are clinically relevant, simulated cluster properties must be compared to true clusters. While it is possible to perform *ex-vivo* tissue analysis to characterize microsphere distributions in treated tissues, current methods are manual and very time-consuming and make 3D cluster characterization difficult. Accordingly, previous analyses of microsphere clusters have only examined small areas of tissue, potentially underestimating cluster extents. The ability to detect 3D microsphere locations in larger tissue blocks could provide a better understanding of the quantity and variety of microsphere clusters in normal liver tissue.

With a better understanding of the microsphere clusters and dose distributions, it could be possible to better predict the effect of different treatment plans on normal liver tissue and thus improve patient outcomes.

The ability to create a personalized computational model of the hepatic arterial tree and simulate the administration of different total and specific activities could be a useful tool for doctors to optimize treatment plans.

1.2 Organization

This dissertation first explains background information necessary to understand the research undertaken in support of the thesis. Following that are chapters describing novel work to improve treatment planning tools. Those chapters have either been published, submitted for peer review, or are being prepared for publication.

Chapter 2 reviews the properties of the liver that make it a common site for primary and metastatic cancers, and a challenging target for other cancer treatments. The chapter also describes the unique anatomical features of the liver and related cancers that make RE a viable treatment strategy, and briefly explains the relevant physics and biological impacts of radiation-based treatment methods. The basic features of the two FDA-approved RE devices are summarized. Information relevant to micro-computed tomography (CT) imaging of small, highly attenuating objects (such as glass microspheres containing yttrium) is also presented with important details from previous work detecting microspheres at the scale of a few dozen microns.

Chapter 3 describes initial work to develop a model of the hepatic arterial tree that is both physically realistic and sufficiently detailed to allow particle infusion modeling. It shows simulated dose maps that are qualitatively similar to those observed in patient dose maps created using PET imaging.

Chapter 4 explains how 3D glass microsphere locations can be estimated in reasonably large tissue samples using micro-CT and standard morphological image processing algorithms without requiring the tedious specimen slicing, staining, and scanning most commonly used to investigate microsphere localization.

Chapter 5 shows how glass microspheres cluster in normal porcine livers using the microsphere location estimation algorithm. It then describes how the particle transport and trapping model from chapter 3 was adapted to produce clusters similar to those measured in the normal porcine livers.

Chapter 6 reviews the novel findings of this work and suggests potential avenues of future research.

Chapter 2

Background

In order to provide context for the work undertaken for this thesis, this chapter describes relevant background concepts.This work focuses on radioembolization of liver cancer, and thus an understanding of the anatomical and physiological properties of the liver is beneficial. Thus, the basic function and form of the liver are summarized. A brief discussion of the pathology and treatment of liver cancers is undertaken prior to the introduction of RE as a promising therapy. The biological effects of both embolization and radiation are reviewed, with particular attention paid to the interactions of radiation with tissue from the scale of individual atoms to the full liver.

Comparisons between the maximum tolerable absorbed dose (MTAD) of normal liver tissue treated with RE and more uniform absorbed dose delivery methods suggests that spatial clustering of microspheres is relevant to predicting the biological impact of RE treatments. Due to the composition of microspheres used for some RE treatments and the inadequacy of current methods for analyses of microsphere clustering in large tissue samples, micro-CT imaging of tissue with embedded microspheres is suggested as a faster and simpler microsphere detection method. Therefore, a discussion of CT imaging procedures and properties that are relevant to the proposed use case is also provided.

2.1 Liver anatomy

A major focus of this dissertation is radioembolization of liver cancer. This refers to the delivery of microspheres through the hepatic vasculature to their eventual trapping locations in the liver. Unique characteristics of the liver and the liver vasculature determine where they are trapped. How radiation from the decaying radionuclides in the microspheres is absorbed in the liver tissues determines the liver toxicity. It is thus important to have some understanding of liver anatomy and vasculature

The liver fulfills many functions within the body, from synthesizing glycogen, blood proteins, and vitamins to removing dead or damaged cells and toxins [16]. It also acts as a blood reservoir, able to store or supply excess blood in response to changes in blood pressure due to the liver's highly capacitive, heavily perfused cells [17]. The liver is unique among the visceral organs in that it has a dual blood supply. It receives highly oxygenated blood from the hepatic artery (HA) and nutrient-rich blood from the portal vein (PV), and the flow from both vessel trees exits via the hepatic vein. Nearly 80% of hepatic blood comes from the portal vein, while the remaining 20% is supplied by the hepatic artery [18].

The liver can be divided into 8 Couinaud segments, which are defined as portions of the liver perfused by different branches of the PV [19]. Typically, the HA branches similarly [20]. As the PV ramifies down to the level of the smallest venules, the HA branches into hepatic arterioles. At the lowest level, the portal venules and terminal hepatic arterioles (THAs) form portal tracts that perfuse the smallest functional units of the liver.

Each portal tract receives blood from THAs or portal venules, usually both [21]. The blood flows away through three sinusoids, which are a type of capillary with a specialized lumen (vessel lining) that allows the blood-borne molecules to enter and exit nearby parenchymal cells. Those cells include Kupffer cells, which are macrophages that destroy damaged cells and rid the body of toxins, and hepatocytes, which process nutrients carried by the portal venous system from the stomach and intestines into glycogen and synthesize necessary vitamins. The blood then drains into the centrilobular vein that terminates each sinusoid. The centrilobular veins merge into the hepatic vein and join the inferior vena cava, which connects to the right atrium of the heart [18].

There are two ways to interpret the smallest functional units of the liver: the lobule model and the acinus model, depicted in figure 2.1. Lobules are approximately shaped as hexagonal prisms with a portal tract at each corner of the hexagon and a centrilobular vein at the center.

The acinus model is similar to the lobule model, except it is centered on the portal tracts and better reflects the metabolic zonation of the sub-units [22]. In this work, the THA-centered acinus model is used as it is a more convenient model of the HA structure.

Each acinus operates in parallel with the other acinii, which means that regular hepatic function can continue even with partial liver damage [11]. The liver can also regenerate to replace resected cells, though liver function can be compromised in cases where patients have existing liver diseases such as cirrhosis [23].

Due to the liver's role in removing damaged cells and filtering toxic substances from the blood [22], it is commonly involved in both primary cancers arising from damage to liver tissues and metastatic cancers from circulating cancer cells [6]. Patients without cirrhosis presenting with a single, accessible lesion are candidates for resection, or surgical tumor removal [24]. Liver transplantation can be employed if the patient has less than 4 small lesions, though the availability of donor livers prevents this from being used as commonly

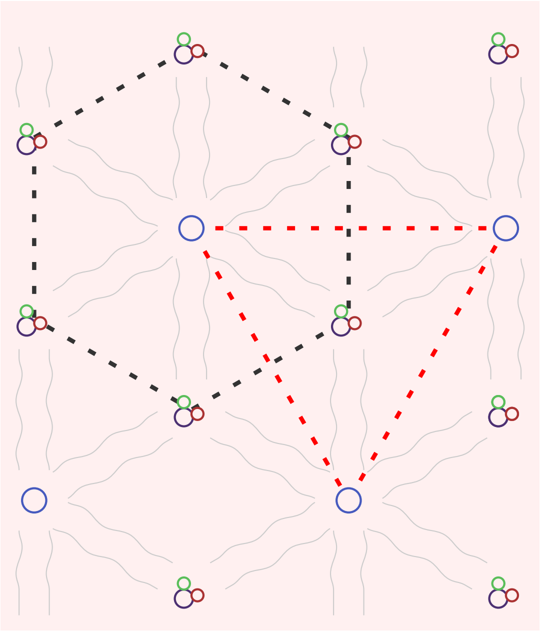

Figure 2.1: Liver microanatomy. The black hexagon represents a lobule, while the red triangle represents an acinus. In this simplified depiction, each corner of the hexagon coincides with a portal triad. Portal triads contain portal venules, hepatic arterioles, and bile ductules. In most portal triads, there are more than one terminal arteriole, and sometimes portal venules or hepatic arterioles are not present.

as would otherwise be indicated. Unresectable cancers can also be treated with radio-frequency ablation [24]. Other therapies, such as RE (discussed below) are considered palliative, not curative. However, some palliative therapies show promise when used in conjunction with the curative therapies listed above.

2.2 Radioembolization

2.2.1 Embolization

Cancers that have developed in or metastasized to the liver receive a majority of flow from the highly oxygenated hepatic arterial blood [19]. This tumoral preference for arterial blood also suggests a form of treatment that interrupts the supply of arterial blood to tumors by injecting particles into the arterial flow that trap in the smallest vessels at or near the tumors. The smallest hepatic arterioles have an average diameter of $11.8\,\mu\mathrm{m}$, so the spherical particles intended to trap in such vessels are sized at a couple dozen $\mu\mathrm{m}$ in diameter. These spheres are known as microspheres. Embolizing the smallest branches of the HAT reduces the supply of blood to tumors perfused by it, while normal tissue is able to survive on just the portal-venous flow and the remaining arterial flow.

In addition to depriving tumors of oxygen-rich blood, microspheres used for embolization are often labeled to deliver therapeutic agents to the cancer. For example, in trans-arterial chemoembolization (TACE), the microspheres contain chemotherapeutic agents that are eluted by the blood, thus delivering cancer-fighting drugs selectively to the tumors. [24–26]. Of interest in this work is that the microspheres may also contain radioactive nuclei. When these nuclei decay they deposit energy in neighboring tissues, compounding the physical effects of embolization. [12].

2.2.2 Radiation

Radiation damages tissue in different ways depending on the radiation type and energy. Ionizing radiation is radiation that can cause electrons to be ejected from atoms and thus disrupt chemical bonds and molecular structures. The three types of ionizing radiation most relevant to this work are beta particles, gamma rays, and x-rays. This introduction will ignore non-ionizing interactions of radiation and matter.

Beta particles are charged particles that are produced by radioactive nuclei during beta decay [27]. A β^- particle is an electron, and therefore negatively charged. The most common β^- particle interaction that is of interest here is for a β^- particle to transfer energy to atoms in the object via collisional transfer. This transfers energy from the particle to either the full atom in the form of kinetic energy, or to an orbital electron, which either moves to a higher energy orbital or, if sufficient energy is imparted to overcome the binding energy of the atom, the electron is ejected and the atom is ionized [27]. Another common occurrence, depending on the particle energy and surrounding medium, is that the β^- particle is deflected by the nucleus of the atom; the momentum lost in this deflection is emitted as bremsstrahlung, or braking, radiation. The larger the angle of deflection, the higher the energy of the emitted photon. While bremsstrahlung interactions do not directly ionize matter, the photons produced by it can. This is also true of the photons emitted when electrons in higher orbitals return to their ground state.

The other type of charged particle of interest to this work is the β^+ particle, which is a positron created by beta decay. These travel through matter, losing energy, and, when almost at rest, annihilate by interaction with electrons. The annihilation results in the emission of two 511 keV photons traveling in approximately opposite directions [28]. If the β^+ particle interacts with a bound electron, annihilation directly ionizes that atom. The 511 keV photons produced can also ionize further matter, through photon-matter interactions discussed below.

Gamma rays are photons emitted from a nucleus during radioactive decay, while x-rays originate from atomic electrons [27]. Regardless of the point of origin, these photons can directly or indirectly ionize matter through the photoelectric effect, Compton scattering, or pair production. The particular interaction depends on both the incident photon energy and the composition of the participating medium.

While Compton scattering is more common in tissue at energies used for x-ray scans, because all incident photon energy is absorbed in the photoelectric effect, photoelectric interactions are still a substantial cause of ionizations [27].

Depictions of these interactions are shown in figure 2.2. Photons and free electrons produced in these interactions may continue to further ionize other atoms in secondary interactions. Further, when orbital electrons are ejected and replaced with other bound electrons, another photon is emitted, which may result in additional ionizations. The likelihood of a photon being absorbed or scattered by material in its path depends on the energy of the photon and the composition and density of the material. Photons are much more likely to interact with materials having nuclei with larger numbers of protons (referred to as higher-Z materials). A photon beam traversing matter that absorbs some fraction of the incident photons is referred to as an attenuated beam [28].

The different radiation interactions that can ionize matter are depicted in figure 2.2.

The amount of energy deposited into a given mass of tissue by any of these interactions is referred to as the absorbed dose, which has units of Gray (Gy), a derived unit equal to J/kg. The higher the absorbed dose in a volume of tissue, the greater the chance of biological effects, such as radiation damaging the cell structures or DNA. Different forms of ionizing radiation have different biological effects depending on how much energy they deposit per unit distance, referred to as the linear energy transfer (LET). Beta particles have relatively low LET and thus require many ionizations to kill cells [29].

In the US, both commercially available microsphere varieties contain ^{90}Y;

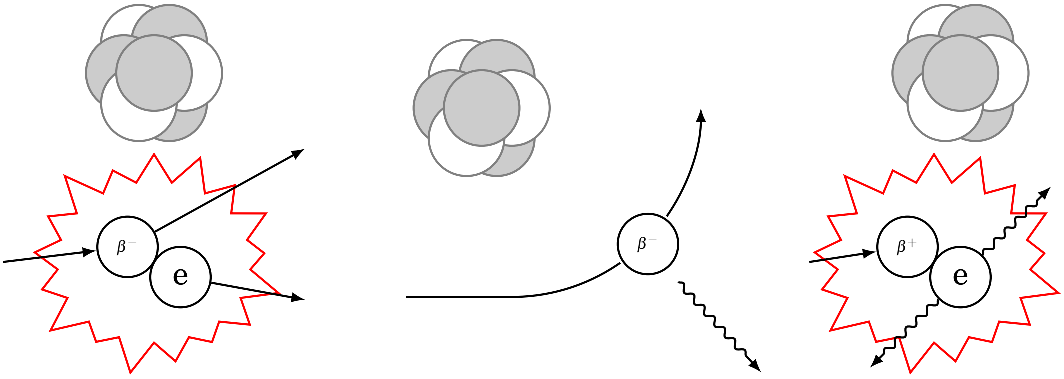

(a) Collisional transfer **(b)** Bremsstrahlung **(c)** β^+ Annihilation

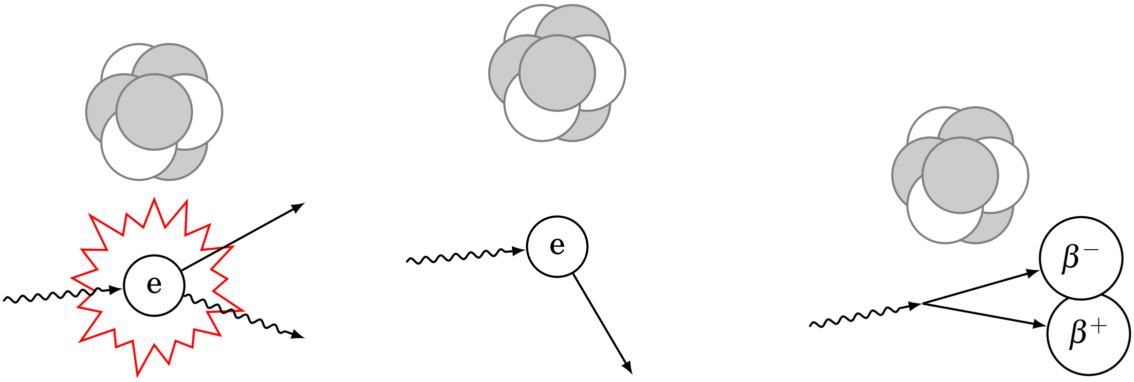

(d) Compton Scattering **(e)** Photoelectric Effect **(f)** Pair production

Figure 2.2: Relevant ionizing interactions of radiation with matter. The top row shows interactions of charged particles with matter and the bottom row shows interactions of photons with matter. (a) An incoming beta particle transfers energy to free a bound electron. (b) A β^- particle passing near a nucleus can have its trajectory affected and emit an x-ray whose energy depends on the amount of deflection. (c) A β^+ particle can collide with an opposite-charged particle and annihilate, converting the particles' mass into two 511 keV photons traveling in opposite directions. (d) A photon impact that transfers sufficient energy to a bound electron will eject the electron and adjust the photon trajectory. (e) A photon is completely absorbed by an orbital electron and the electron is ejected. (f) When a very high-energy photon approaches a nucleus, it can convert into an electron-positron pair that cause further ionizations in the manners described above.

its decay results in energy deposition in tissues near microsphere trapping locations. ^{90}Y is a radioactive isotope of yttrium with a half-life of 64.1 hours that emits a β^- particle while transitioning to stable ^{90}Z. ^{90}Y has a peak beta particle energy of 2.28 MeV and an average energy of 0.937 MeV [19]. The maximum distance an ^{90}Y beta particle travels in tissue is about 11 mm and the average distance is about 4.1 mm [12]. Ninety percent of the energy emitted by ^{90}Y is deposited within 5.3 mm [19], which means that trapped microspheres emitting radiation damage nearby tissues while sparing tissues that are farther away [19]. The activity of a sample of a radionuclide is measured in disintegrations-per-second, or Becquerels (Bq) and refers to how frequently a disintegration occurs based on the radionuclide quantity and half-life. A radionuclide with a short half-life deposits more energy more quickly than a radionuclide emitting the same radiation with a longer half-life.

2.2.3 Microsphere types

In the US, two types of microspheres are used to treat different liver cancers, SIR-Spheres (SIRTEX Medical Limited) and TheraSphere (Biocompatibles UK Limited).

SIR-Spheres are polymer-resin microspheres with an average diameter of 32 µm that are labeled with ^{90}Y. SIR-Spheres have an activity of 50 Bq each at calibration time and must be used within 24 hours of that time. There are several suggested methods for calculating the correct administered activity that consider the liver volume, tumor burden, and more. SIR-Sphere treatment administration is an extended process where some microspheres are delivered to the HA, the arterial system is checked for stasis (a state where microspheres will no longer flow through the HA), and then more spheres are administered if stasis has not been reached. The low activity per SIR-Sphere means that tens of millions of microspheres are necessary to provide sufficient absorbed dose to targeted tumors.

TheraSphere are microspheres composed of glass doped with ^{90}Y and have a slightly smaller average diameter of 25 µm. The activity per TheraSphere is substantially higher, at 2500 Bq per sphere. This higher activity means that fewer microspheres are necessary to achieve a high absorbed dose of radiation. Manufacturer-recommended treatment plans consider only the mass of the treated liver volume when determining the administered activity. Also, in contrast to SIR-Spheres, TheraSphere treatments are typically allowed to decay until the manufacturer-supplied quantity of microspheres has the desired activity and is then injected in a single bolus [19]. Both types of microspheres are bio-compatible, but not biodegradable, meaning that they trap permanently and only damage tissue via emitted radiation and ischemic effects due to embolization [30].

2.2.4 Microsphere-based tissue damage

After microspheres trap in small vessels, the emitted beta particles deposit energy into nearby tissues [30]. They damage cells in two ways: first by directly damaging a cell's DNA or other sensitive structures [31], and second by ionizing molecules in cells (such as water) to create free-radicals that in turn damage DNA, membranes, and other cellular structures [32]. Cells usually have mechanisms to repair sub-lethal damage, but the typically fast proliferation of tumor cells can actually decrease their ability to tolerate radiation-induced damage compared with normal cells [32], increasing the effectiveness of radiation treatments.

A common concern when using ^{90}Y-labeled microspheres is that a hazardous number of microspheres could pass through the hepatic artery into the hepatic venous system without trapping in the smallest liver vessels. This can happen due to variations in vascular morphology or shunting caused by erratically grown tumor-supplying vessels. Spheres that pass through the liver will continue circulating through the vascular system and embed in the lungs, which are more radio-sensitive than the liver [33], potentially resulting in radiation pneumonitis [12, 33]. The concern about lung damage is sufficiently serious that TheraSphere-based treatment plans call for pre-therapy measurement of lung shunting using macroaggregated albumin (MAA), a protein-based particle, that is labeled with $^{99\mathrm{m}}$Tc, a radionuclide that emits gamma rays with ideal properties for nuclide medicine imaging. Like microspheres, MAA is administered trans-arterially and mostly traps in the liver. The accompanying technetium emits photons that can be detected to show where the MAA has trapped. If high levels of MAA are detected in the lungs, the total administered dose is either reduced or the treatment plan is altered to avoid serious effects due to radiation damage in the lungs [19]. The trapped albumin particles erode after a few hours and are excreted [19].

While MAA particles are similar in size to TheraSphere and SIR-Spheres and have been suggested as a therapy planning tool [9, 13, 34], they are not ideal surrogates for those microspheres due to differences in observed particle distributions [35]. This is thought to be caused by differences in particle size, shape, and density [19], as well as frequent differences in catheter placement during infusion [36].

Other hepatic treatments involving external sources of radiation have been studied, such as EBRT, where one or more poly-energetic x-ray beams are focused on a tumor site [37]. The treatments are often administered over several sessions to reduce the chance of toxicity [38], as a decreased dose rate results in less tissue toxicity due to normal cells' ability to repair sub-lethal damage when compared with tumor cells [29, 37]. However, the average MTAD for EBRT is still much lower than what is possible using RE [10, 37]. This is likely due to the uniform deposition of dose in EBRT [8], the tendency of microspheres to aggregate into clusters [9], and the structure of the liver microanatomy [11].

Currently, trans-arterial treatments such as RE, TACE, and trans-arterial embolization (TAE) are considered palliative, not curative. However, RE has been used to downstage liver tumors and enable the use of curative options such as resection and increase patient survival [39–41].

Optimal RE treatment plans maximize the absorbed dose in tumor tissues without inducing toxicity in normal liver or other adjacent tissues. Such plans maximize the probability of tumor control and may enable curative treatments. Understanding the distribution of microspheres is important in creating optimal treatment plans, as that can predict useful measures such as mean tumor dose and the probability of normal liver toxicity. However, current technologies for estimating microsphere quantities and locations, e.g., using SPECT or PET imaging, are not sufficient to capture the dose heterogeneity with sufficient resolution to predict normal tissue toxicities.

2.3 Microsphere detection

Because sufficiently accurate *in-vivo* detection of microsphere distributions using SPECT or PET imaging is not possible, the ability to examine tissue *ex-vivo* can still yield important information about dose gradients and tumor control. Traditional methods of sample preparation involve embedding a small tissue sample in paraffin, dividing the sample into thin slices a few micrometers thick, staining the slice with a dye to increase visual contrast, and then scanning each slice via optical microscopy and recording the locations of microspheres [42]. This is repeated for all slices. Sample slice thickness and microsphere thickness must be considered when determining microsphere locations in the direction normal to the slice plane to prevent severed portions of resin spheres from being counted in multiple sections [43]. Glass microspheres are not severed using typical microtome-based slicing methods, but they can be pushed out of a sample if the slices are too thin. However, slices that are too thick will not capture the 3D microsphere locations with uniform fidelity. Due to the very labor- and time-intensive process of slicing, staining, sectioning, scanning, and scrutinizing samples, this method is only applied to small tissue regions. A more useful method to examine full microsphere distributions would be able to image whole tissue samples without requiring so much sample preparation.

2.3.1 CT image formation

CT image acquisition and reconstruction creates a three-dimensional representation of objects being scanned using their different attenuation properties. The fundamental basis of CT is shared with x-ray imaging. A fan- or cone-shaped beam of x-rays passes through a 3D object and is measured at the far side of the object at fixed intervals by a two-dimensional x-ray detector, depicted in figure 2.3. As the photons pass through the object, some are scattered and some are absorbed. The intensity is measured at each detector location and the same set of measurements is taken from several different angles around the imaged object. Each set of measurements is known as a projection, and a large set of projections can be used to estimate the attenuation values within the object.

An expression for the intensity of the x-ray beam on a point of the detector is given by Prince and Links [27] as

$$I(x,y) = \int_0^{E_{max}} S_0(E')E'exp\left[-\int_0^{r(x,y)} \mu(s;E',x,y)ds\right]dE', \tag{2.1}$$

where x and y are the coordinates of the point on the detector, S_0 is the energy spectrum of the incident x-rays, E_{max} is the maximum energy of that spectrum, $r(x,y)$ is the length of the line between the x-ray source and detector location (x,y), and μ describes the fraction of x-rays expected to be attenuated at each point in the 3D object. The integral along the ray between the source and detector location (x,y) projects the attenuation values along that ray.

Equation (2.1) captures the fact that x-rays emitted from traditional sources will have a spectrum of energies, not just one, and that different materials will attenuate differently depending on the incident photon energy. However, due to the complexity of working with (2.1), the equation is simplified using the

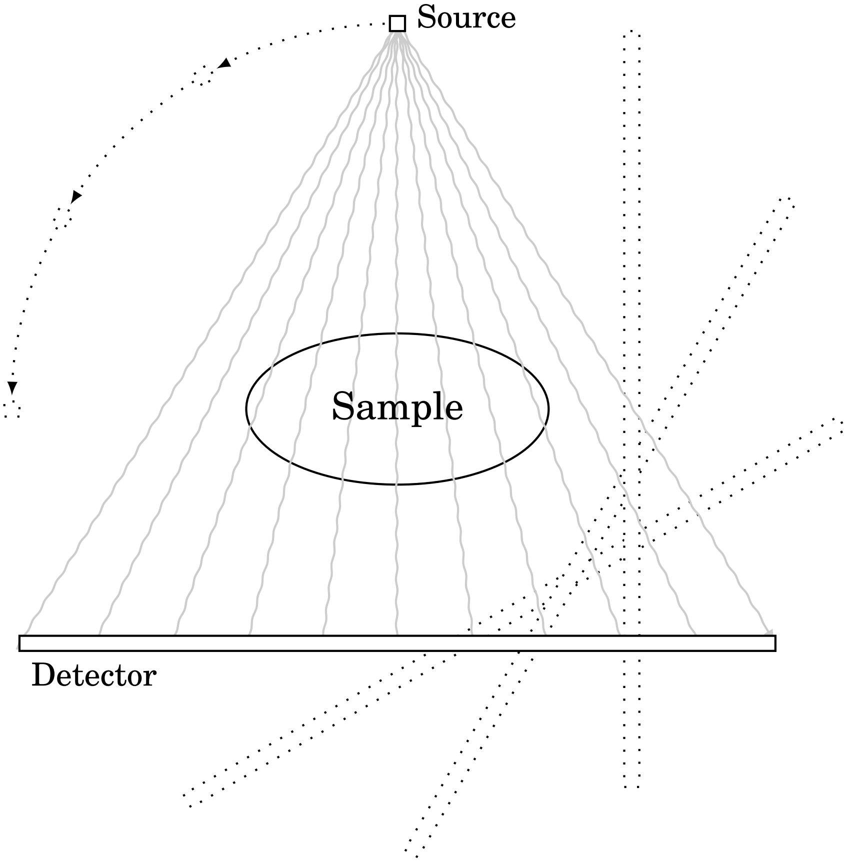

Figure 2.3: A simplified model of a 2D CT scanner with fan-beam geometry. The source and detector are on opposite sides of the sample being imaged; an x-ray projection is recorded, and the source and detector are rotated and projections are acquired at a set of projection views, usually taken at small, evenly spaced angles. The angle between projections is exaggerated here for clarity.

assumption that the source is emitting a mono-energetic beam at an energy that will produce the same measured intensity as the actual poly-energetic beam [27]. This yields the equation

$$I(x,y) = I_0 \exp\left[-\int_0^d \mu(s;\bar{E})ds\right], \tag{2.2}$$

where I_0 replaces S_0 as the intensity of the beam at energy $\bar{E}$ and d is the length of the line between the source and point (x,y).

The goal of CT reconstruction is to estimate $\mu(\cdot)$ using multiple projections taken from different angles around the body. If I_0 is known, the attenuation of all material between the source and the point (x,y) can be measured using (2.2):

$$\int_0^d \mu(s;\bar{E})ds = -\log\left(\frac{I(x,y)}{I_0}\right) \tag{2.3}$$

This basic measure is made along all the rays between detector pixels and the x-ray source for each projection angle around the imaged object. This yields a set of projections taken at many different angles around the object. It is possible to reconstruct the attenuation values $\mu(\cdot)$ of each point in the object using those projections with a reconstruction algorithm based on the inverse Radon transform. For cone-shaped x-ray beams, such as those used for micro-CT, the Feldkamp reconstruction algorithm is the most well known and commonly used [27].

2.3.2 Micro-CT image degrading factors

There are several sources of image degradation in CT due to physical limitations of the system and algorithmic approximations. Some knowledge of how the source generates x-rays and how they are detected is necessary to understand those degradations.

The x-ray source in CT scanners, the x-ray tube, consists of a cathode that emits a stream of electrons and an anode that the electrons bombard, producing x-rays mostly through bremsstrahlung interactions [44]. The cathode assembly is negatively charged and contains a filament composed of tungsten that, when a current is induced, produces free electrons through thermionic emission [27]. The anode is positively charged and thus attracts electrons from the cathode. This flow of electrons between the cathode and anode is referred to as the *tube current* [44]. The anode is composed of materials with large, high-Z nuclei to increase the chances that the electrons will interact and produce bremsstrahlung radiation, and to withstand the heat deposited in it by the electron interactions. The quantity of x-rays produced depends not only on the tube current, but on the electric potential (voltage) between the anode and cathode. This difference is called the *tube voltage* and the higher it is, the higher the energy and quantity of the generated photons. A simplified depiction is shown in figure 2.4.

This process by which x-ray beams are created produces a random number of photons traveling in the direction of any point on the detector. The absorption of any photon within the sample or detector is likewise probabilistic. This means that even uniform materials scanned via CT will have a non-uniform appearance. In fact, the number of photons interacting with the detector at each projection can be modeled as a Poisson random variable, which has a variance equal to the mean value.

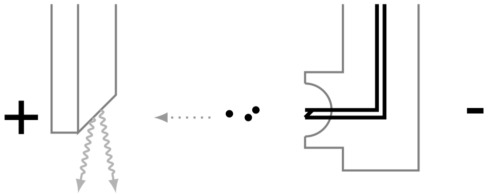

Figure 2.4: A demonstration of electrons moving from the tungsten filament of the cathode and flowing to the positively charged anode. The anode is composed of high-Z, heat-tolerant materials such as tungsten and molybdenum that are likely to produce x-rays when electrons are incident. The part of the anode at which the electron flow is focused is the *focal spot*. The anode is sloped at the focal spot to avoid anode-absorption of x-rays emitted in the correct direction. However, the x-ray beam directed at the detector is still not uniform so additional hardware (not shown) is necessary to filter and shape the resultant x-ray beam.

Reconstruction algorithms require that a windowed filter be applied to the data to avoid amplifying noise in the reconstructed image [45]. This process transforms the uncorrelated Poisson-like noise in each projection into correlated noise, which changes the noise texture in the reconstructed image, as shown in figure 2.5.

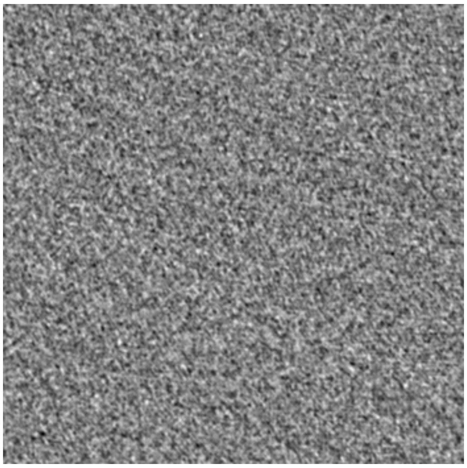

Figure 2.5: Example of CT noise patterns visible in a uniform water phantom.

In addition to the noise texture visible in image reconstructions, there is a limit to the distance between distinguishable objects in CT images. This distance is known as the spatial resolution of the system [27]. While two objects less than a detector pixel distance apart can obviously not be distinguished, there are many important factors affecting the spatial resolution of a CT imaging system, such as the thickness of the detector, the size of the focal spot of the x-ray tube, the physics of photon propagation, and the properties of the reconstruction algorithm [27, 45].

CT detectors contain a grid of light-sensitive elements that allow the two dimensional detection of incident photons. These elements are much more sensitive to lower-frequency light, and so a thin scintillator is typically placed between the detector and the x-ray source. The scintillator converts incident x-rays into lower-energy photons through fluorescence and decreases the amount of x-ray exposure necessary to create a projection by increasing the detector sensitivity. The sensitivity of the detector is directly related to the thickness of the scintillator, as higher energy photons are more likely to be stopped. However, the thickness of the scintillator also directly affects the resolution of the system. The depth of the x-ray interaction in the scintillator affects how many detector bins measure incident photons, and consequently, how blurred an incident photon will be.

Another cause of resolution degradation is that the x-rays are emitted from an area source, not a single point. While the design of the x-ray tube attempts to focus the tube current on a single focal spot of the anode, there are invariably deviations in impact location that cause x-rays to be emitted from different locations around the focal spot. Geometrically, this source location uncertainty increases the blurring observed at the detector.

This effect is exacerbated by magnification that occurs the closer the imaged object is placed to the x-ray source. This effect is particularly noteworthy in micro-CT scanners, which deliberately move the imaged object closer to the x-ray source so that smaller volumes can be imaged with larger detector pixel sizes.

Finally, when photons pass through the sample, some will be absorbed due to the photoelectric effect, some will be scattered, and some will pass through the sample and be detected. Some scattered photons may still arrive at the detector and result in incorrect incident intensity measures in the projections. For CT systems imaging large volumes, detections of scattered photons can be mitigated by including anti-scatter grids that attempt to attenuate photons not traveling along rays from the source at the cost of decreasing detector sensitivity, but for micro-CT systems imaging smaller volumes, this is usually omitted due to the very small detector pixel size.

While noise and system blurring are very common image degrading factors, others are also relevant to this work and thus require some explanation. Equation (2.2) used an approximation that x-ray beams are mono-energetic in order to make estimating attenuation values at each voxel of the reconstructed image tractable, the x-ray beams produced by bremsstrahlung interactions are actually poly-energetic. As a poly-energetic beam passes through a thick sample, the lower-energy photons are relatively much more likely to be attenuated than higher-energy photons. This results in more photons arriving at the detector than would be expected for mono-energetic x-ray beams, which means that the attenuation of the penetrated media will be underestimated. This phenomenon is referred to as *beam hardening*. A common mitigation technique uses copper and aluminum filters positioned between the x-ray source and the sample to "pre-harden" the x-ray beam by removing low-energy photons before they reach the sample.

Additional artifacts include streaks caused by attempting to estimate $\mu(\cdot)$ with insufficient projections and rings caused by broken or incorrectly calibrated detector elements.

2.3.3 Micro-CT microsphere detection

Glass microspheres (like TheraSphere) that are composed of borosilicate glass doped with yttrium have a much higher attenuation coefficient than resin-based spheres (such as SIR-Spheres) or tissue. While the average diameter of the microspheres is very small compared to the resolution of clinical CT scanners, some micro-CT scanners have the ability to resolve even smaller objects [46]. This suggests that micro-CT imaging of tissue with embedded microspheres should have high contrast between voxels containing microspheres and those without.

Marxen *et al.* demonstrated the feasibility of imaging silver- or gold-coated polystyrene beads with approximately the same diameter as the glass microspheres considered in this work [47]. However, the described method imaged only a small volume and did so using twelve-hour (and thus very low-noise) scans. Attempting to image similar objects using the same acquisition parameters on a larger tissue sample would require prohibitively long scans. Issues with image resolution were also generally ignored. However, the ability to characterize microsphere clusters using micro-CT could lead to improved understanding of microsphere and dose inhomogeneity, and eventually improved treatment plans, by studying the results of actual treatments in resected liver tissue.

Chapter 3

Development of a Customizable Hepatic Arterial Tree and Particle Transport Model for Use in Treatment Planning

3.1 Introduction

The use of RE for treating metastatic and primary liver cancers is increasing due to its ability to deliver high treatment doses to tumor tissue and low doses to normal liver parenchyma, thus reducing liver toxicity compared to EBRT [7].

Treatment is performed by inserting a catheter into the HA and administering radioactive microspheres that embolize the microvasculature and deliver radiation near the location of embolization. Due to the tumors' primary use of arterial blood [7], particles are likely to be trapped near and deliver a high absorbed dose to tumors while sparing normal liver structures.

Other approaches, such as fractionated EBRT, induce toxicity at much lower doses than RE, and this may not allow a fatal dose of radiation to be delivered to tumors [19]. Optimal treatment plans for RE must deliver sufficient dose for tumor control while avoiding complications such as radiation-induced liver disease due to excessive dose to normal tissues. Treatment planning for RE using glass microspheres principally uses the total mass of the treated liver volume to calculate the mean dose [48]. This planning method aims to deliver a desired average dose to the treated volume and does not account for tumor burden, the ratio of microspheres trapped in tumors versus normal tissues, and their effects on dose heterogeneity. Thus, dose delivered to tumors varies across patients, and this can result in a lower probability of tumor control due to under-dosing of the tumor [34]. The calculation of dose to normal liver tissue is complicated by the non-uniform distribution of microspheres within that tissue and the unique microstructure of the liver itself [11].

Because of the relatively short range of the ^{90}Y beta particles and their nonuniform distribution in the anatomy, it has recently been suggested that the dose at a microscopic level is highly non-uniform, and that this affects the radiation toxicity of normal tissues [11]. Accurately predicting the dose to normal liver tissue at a microscopic level through modeling of patients' liver microanatomies could allow dose adjustment and improve the outcomes of patient treatment. In order to effectively model particle distribution within a given patient's vasculature, a realistic model of that vasculature is required. However, at present there is no method to map the microvasculature *in vivo*. Also, there are differences in the distribution of particle diameters that may affect the final trapping locations of spheres within the microvasculature. The details of this trapping depend, in principle, on details of the vessel diameters, blood pressure, and mechanism of trapping.

Bézy-Wendling *et al.* proposed a method to create a realistic representation of hepatic vasculature based on measured physical properties and an optimality criterion that minimized local vessel volume [49]. The method uses macrocells to incrementally extend an initial vascular tree to perfuse an existing liver shape. The vessels in the generated tree split and taper realistically after each bifurcation from the proper hepatic artery (PHA) to the macrocell connection points.

In their work, however, vessels were generated down to regions two hundred times larger than the size of a macrocell representing a terminal arteriole [30]. At this scale, the terminal vessel diameters are larger than the average diameter of the infused microspheres in RE [50]. Also, without generating vessels down to dimensions of the THA diameters, it is difficult to check the validity of the tree generation method as most data have been collected for initial and terminal vessels. Also, if the vessel diameters in the resulting vascular tree model are larger than the sizes of the infused particles, the tree will not be useful for modeling the trapping of microspheres at a microanatomical scale.

Walrand *et al.* have developed a model of the liver microanatomy, the hepatic arterial tree, and the microsphere infusion process for high-activity, glass microspheres [10, 11]. The tree was generated using an initial hepatic arterial tree supplying the eight liver segments. Those segments were filled with hexagonal prisms that represent the lobule, a functional unit of the liver with blood flowing in at each corner through portal tracts containing one or more THAs and portal venules [18]. To generate a tree from the THAs, each arteriole was chosen at random and connected to the nearest existing vessel that would not result in retrograde flow. Blood flow in each vessel was determined based on the number of terminal arterioles supplied by the vessel or its descendants. This model did not estimate the diameters of any intervening vessels nor take into account blood flow or pressure differentials when generating the tree.

Walrand *et al.*'s particle trapping model assumed that all particles are trapped in THAs and that particle flow at bifurcations is probabilistic and based on both flow and the relative geometry of the child vessels. Simulated images of the activity distribution after a simulated RE procedure had a texture that was qualitatively similar to that observed in PET/CT images. However, the tree produced by this method does not follow observed physical properties. This may impact the heterogeneity of particle and dose distribution. Additionally, the assumption that each particle arrives at a terminal arteriole is unlikely given the range of diameters of microspheres [48] and the measured diameters of the arterioles [21]. Högberg has demonstrated that resin microspheres, which have diameters similar to glass microspheres, are frequently trapped in non-terminal vessels [51].

In this work, we propose a method to generate a vascular tree using a liver volume and the larger branches of the hepatic arterial tree that can be estimated from patient scans. The simulated tree conforms to relevant physical laws and can be adapted to match measured pressure differentials, blood flows, viscosities, and vessel diameters. The blood flow patterns and pressures can be customized for individual patients; e.g., using data from patient scans or measured via a catheter. We also propose a new method to model the infusion and trapping of embolizing particles in those trees that considers the diameters of both the particles and trapping vessels. These can be used to produce estimates of the particle distribution that could be useful for exploring the microscopic dose distribution in normal liver tissues and predict normal tissue dose on an individualized basis.

3.2 Methods

In this work, we have developed a method to generate a hepatic arterial tree from the PHA to individual THAs. This method uses the macrocell-growth algorithm described by Bézy-Wendling *et al.* [49]; various model parameters are adjusted dynamically during tree growth to produce desired quantities of interest such as THA diameters. As will be described below, the binary trees generated using this method conserve matter, conform to Murray's law at all bifurcations, and follow Poiseuille's law within each vessel.

3.2.1 Conservation of matter

To conserve matter, the volume of blood flowing into each vessel equals the volume flowing out of its children, or

$$Q_p = Q_{c_1} + Q_{c_2}, \tag{3.1}$$

where Q_p and Q_{c_x} are the volume flow of blood, modeled as an incompressible fluid, passing through the parent and child vessels. At the highest level, the flow from the PHA equals the total volume of blood flowing out of all terminal arterioles. In this work, we chose to have equal flow to each terminal arteriole, though non-uniform flow distributions could be incorporated if there was knowledge of local relative flow, e.g., from perfusion imaging.

3.2.2 Murray's law

Murray's law describes the relationship between the diameters of a parent vessel and its child vessels [13]. For binary trees, it may be expressed as $r_p^\gamma = r_{c1}^\gamma + r_{c2}^\gamma$, where r_p is the radius of the parent vessel, r_{cx}. is the radius of each child vessel, and γ is the bifurcation constant. Murray originally suggested $\gamma = 3$ to minimize the power necessary to provide adequate blood flow [52], but it is generally accepted that γ varies, depending on the type and caliber of the vessels, from 2 in larger arteries near the heart to 3 in smaller vessels [53]. We have chosen γ based on the vessel diameter ratio (VDR), i.e., the ratio of the diameter of the PHA ($4.5\,\mathrm{mm}$ [54]) and the average THA diameter ($11.8\,\mu\mathrm{m}$ [21]). For a balanced binary tree with equal child vessel diameters, the relation between the parent and child vessels may be expressed as a scalar

$$r_p = 2^{\frac{1}{\gamma}} \cdot r_c. \tag{3.2}$$

For a balanced tree with n levels of branching, the VDR is expressed as

$$VDR = \frac{r_{PHA}}{r_{THA}} = 2^{\frac{n}{\gamma}}. \tag{3.3}$$

The value of n may be estimated for a balanced binary tree with the expression $\log_2$ (number of THAs). The number of THAs can either be determined by filling the liver segmentation with THAs or be estimated by dividing the volume of the liver by the volume of a lobule ($1.87 \cdot 10^{-3}$ mL) and multiplying by two, as the six portal tracts of a lobule are shared by three other lobules. Thus, an expression to calculate the bifurcation constant for a balanced binary tree, given vessel diameters and the number of THAs, is

$$\gamma = \frac{\log_2 (\text{number of THAs})}{\log_2 r_{PHA} - \log_2 r_{THA}} \tag{3.4}$$

Trees generated in this work were unbalanced, which affects both n and γ. The error caused by using (3.4) for unbalanced trees was assessed by observing the percent differences in VDR for trees generated with values of γ between 2 and 3.

3.2.3 Poiseuille's law

Poiseuille's law [49] gives the pressure differential (ΔP) between the extremes of a cylinder as a function of the length (l) and radius (r) of that cylinder, and the viscosity (μ) and volume flow rate (Q) of a Newtonian fluid in that cylinder:

$$\Delta P = 8Q\frac{\mu l}{\pi r^4} \tag{3.5}$$

While blood is not a Newtonian fluid [55], and arterial flow is not laminar

[52,53], Poiseuille's law is still commonly used to model physical parameters of individual vessels [49,53]. The choice of Murray's bifurcation constant controls the VDR, but the generated vessel diameters depend on l, μ, ΔP, and Q. The values of these parameters used in this work are justified below.

The length, l, of a particular vessel is not directly controllable using the macrocell-based generation method. Instead, it is dependent on the locations of the PHA and macrocells and on the optimization criteria used to determine vessel bifurcation points, as discussed below.

The viscosity, μ, of blood depends on factors such as the hematocrit, plasma content, and vessel diameter [55]. Bézy-Wendling *et al.* argued that treating blood viscosity as a constant is a reasonable first approximation [49]. Thus, the effects of modeling blood as a non-Newtonian fluid were not considered in this work; we approximated blood as a fluid with constant viscosity of $3.5\,\mathrm{mPa\,s}$ [56].

A wide range of pressures in the PHA and THAs has been measured across populations and within individuals [18,57,58]. In this work, we typically used $98\,\mathrm{mmHg}$ as the pressure at the input of the PHA [59] and $25\,\mathrm{mmHg}$ as the output pressure at each THA [18].

The flow of arterial blood, Q, is also highly variable [59] and depends on both the input blood pressure and the flow within the portal vein [57]. Unless otherwise noted, we adjusted the arterial blood flow to produce an average THA diameter consistent with that reported in the literature.

3.2.4 Tree generation

Vessel trees were generated using the macrocell-based approach described by Bézy-Wendling [49] and Kretowski [59] that simulates the growth of the liver and its vascular tree over a series of 15 cycles. The macrocells represent THAs whose locations are the corners of hexagonal prisms arranged in a lattice as described in the virtual arterial tree by Walrand *et al.* [10]. The growth process starts with an initial segmentation of the hepatic artery and the liver shape. In the work presented here, the liver shape was taken from the XCAT phantom [60] and has volume 1.75 L. The initial hepatic arterial tree was also taken from the XCAT and has 3 branching levels. Both could instead be segmented from patient images. The liver shape is filled with lobules as done for the virtual arterial tree in Walrand *et al.* [10], and the THA locations in the lobules are stored as the potential macrocell locations. The initial tree, liver shape, and macrocell locations are then scaled to one-twentieth of the final model volume. Active macrocell locations are chosen such that the number of macrocells per unit volume is the same for all cycles without being too close together. For the first cycle, then, one-twentieth of the macrocell locations are designated as active and unoccupied. During that cycle, those macrocell locations are occupied through the proliferation of macrocells over a series of subcycles.

During a subcycle, each macrocell has some probability of mitosis (dividing) and apoptosis (dying), as shown in figure 3.1.

At the start of each cycle, every macrocell is tested to determine if it will divide, die, or remain unchanged. A new macrocell is generated for each dividing macrocell, and the new macrocell occupies a nearby, active location, if available, and is connected via a new vessel to the nearest branch of the existing hepatic arterial tree. The connection point is controlled by physical principles that optimize the flow of blood through those vessels and is discussed below. If there are no nearby unoccupied, active locations, then the new macrocell is removed. The order in which new macrocells are processed is random. When a macrocell is marked for deletion, the vessels connecting it to the tree are removed and flow values in parent vessels are recalculated.

The process of mitosis and apoptosis in subcycles continues until the cycle termination criterion is reached. The termination criterion is that more macrocells die than are created in a subcycle, which indicates that nearly all active macrocell locations are occupied. At that point, the current cycle is ended, and the liver volume, hepatic arterial tree, and potential macrocell locations are scaled up linearly to fill a larger liver volume. A superset of potential macrocell locations are identified as before, and a new set of subcycles begins until the cycle termination criterion is reached. These cycles continue until the liver matches its original volume.

During later cycles, when the number of vessels is in the tens of millions,

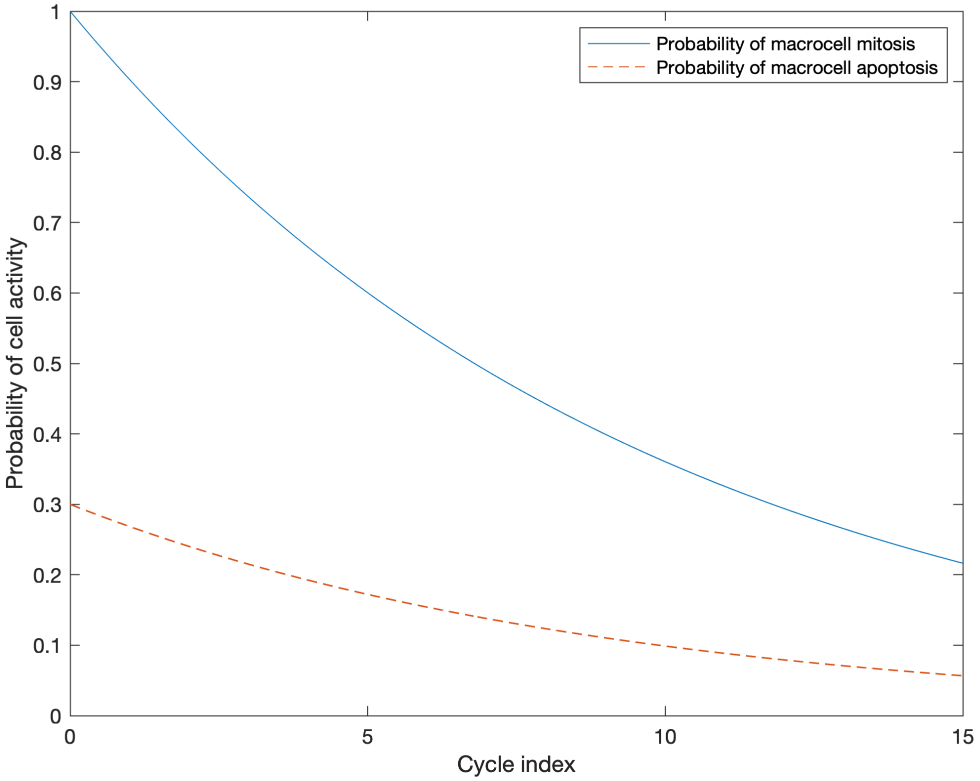

Figure 3.1: Probabilities of macrocell mitosis and apoptosis as a function of growth cycle number. Note that the probability of mitosis is always higher than that of apoptosis, leading to the shape eventually filling as the subcycles progress.

searching for the nearest vessel to a proposed THA location can take a significant amount of time. This was mitigated by storing vessel locations in an octree data structure [61], reducing the complexity of searching from linear to logarithmic.

When macrocells are added to the model, the nearest vessel is bifurcated to supply blood to both the new macrocell and the vessel's previous perfusion area. When this occurs, an optimality criterion determines the location of the bifurcation point [49]. Zamir *et al.* investigated several optimality criteria, including minimizing the power to pump blood through a junction, and minimizing vessel surface area, volume, or shear stress at a junction [62]. However, there is not consensus on which optimality criterion is most physiologically realistic [63]. Bézy-Wendling *et al.* chose to minimize local vessel volume to determine the optimal bifurcation point [49], which minimizes the amount of blood required to perfuse the organ and the time it takes for blood-borne items to circulate [63]. Fung *et al.* chose to minimize the shear stress on vessel walls [64], which has the benefit of determining the bifurcation point based solely on information available to each locally growing vessel [63]. The derivation in [64] supplies a formula for choosing the optimal point for a bifurcation that depends only on the vessel endpoints and the relative flow in each vessel. This reduces the computational effort necessary to choose bifurcation points. Due to the large number of vessels being generated in this work, we minimized the shear stress on vessel walls as described by Fung. During tree growth, the vessel diameters, pressures, and flow rates are periodically computed as described by Kretowski *et al.* [59]. In this method, vessel diameter is the dependent variable and the change in pressure, blood flow, and vessel length are independent variables. Using this method to generate a tree with correct THA diameters requires that the flow (or other variable) be adjusted after construction is finished. The flows are adjusted as follows: After the tree is generated and K macrocells perfused, there is one path from the PHA to each macrocell. For each path, we can write

$$\Delta P_{ALL} = P_{PHA} - P_{THA} = \sum_{i=1}^{n_x} \frac{8Q_{x_i}\mu l_{x_i}}{\pi r_{x_i}^4}, \tag{3.6}$$

where n_x. is the number of vessels in path x, and Q_{x_i},l_{x_i}, and r_{x_i} are the flow, length, and radius of the ith segment of path x. Here we wish to change the total hepatic flow, Q, to achieve a particular average THA diameter without changing any other parameters. Due to (3.1), scaling Q by a factor results in each Q_{x_i} being scaled by the same factor. The result for each r_{x_i} is complicated by the non-linear constraint imposed by Murray's law. If we use the same assumption used in (3.2) and (3.3), we can rewrite (3.6) in terms of r_{THA}, the average terminal radius, as

$$\Delta P_{ALL} = \sum_{i=1}^{n_x} \frac{8Q_{x_i}\mu\, l_{x_i}}{\pi 2^{4(i-1)/\gamma} \cdot r_{THA}^4} \tag{3.7}$$

Equation (3.7) remains balanced if, for any scalar α applied to r_{THA}, each Q_{x_i} (and by extension, Q) is scaled by α^4. The validity of the simplification was tested by comparing the average THA diameter for different Q and ΔP_{ALL} with the predicted diameters, as described below.

3.2.5 Trapping model

In addition to a model of the hepatic arterial tree, we have adapted the particle trapping model developed by Walrand *et al.* to take into account the diameter-distribution of the particles and the diameters of the vessels. The modified algorithm operates by randomly sampling a diameter from the particle diameter-distribution and placing a particle of that size into the initial vessel of the tree. The particle then flows through the tree until it arrives at a vessel that is either too narrow for the particle or is a terminal arteriole. At each bifurcation, the particle randomly enters the left or right child vessel, depending on the vessels' geometries at the bifurcation and the division of blood flow, as described by Walrand [10]. The particle is trapped if both vessels are smaller than the particle diameter, but, if only one vessel is too small, the particle enters the larger vessel. We simulated the effect of embolization by linearly reducing flow through a vessel, in proportion to the number of particles trapped in it, until 50 particles are trapped and flow to that vessel stops. After a particle is trapped and the flow in the vessel adjusted, the flow and bifurcation probabilities are recalculated for the whole tree.

Several 120 Gy whole-liver infusions were modeled for trees generated as described above with average THAs of 11.8 µm. Further 120 Gy infusions were simulated for trees with average THA diameters of 15.8 µm and 18.3 µm to compare the fraction of infused spheres arriving at THAs. All infusions were modeled with particles simulating glass microspheres whose diameter distribution was a truncated Gaussian with mean 25 µm and standard deviation 5 µm [19].

3.3 Results

Estimating the bifurcation constant that produces the correct VDR using (3.4) with 1,868,346 THAs (estimated using liver volume), yielded $\gamma = 2.43$. Trees generated using this method had an average of 1,849,429 macrocells, and each terminal arteriole perfusing a macrocell had, on average, 435 bifurcations between itself and the PHA, which is much larger than the 21 bifurcations necessary for a balanced tree. Figure 3.2 shows that the relative differences between the expected VDRs for balanced trees and the VDRs for generated trees was between 2% and 8% for a range of bifurcation constants. This indicates that (3.4) is a reasonable means to estimate the bifurcation constant, despite the asymmetry of the vessel tree.

Figures 3.3 and 3.4 show the relationship between the average THA diameter and blood flow and pressure differential. Each figure shows the relative error between the actual average THA diameter and the diameter predicted for a balanced tree. In both cases, the error was much less than 1% of the predicted value. This indicates that approximating the relationship between parent and children vessels as a simple scalar, as in (3.2) and (3.7), does not have a signifi-

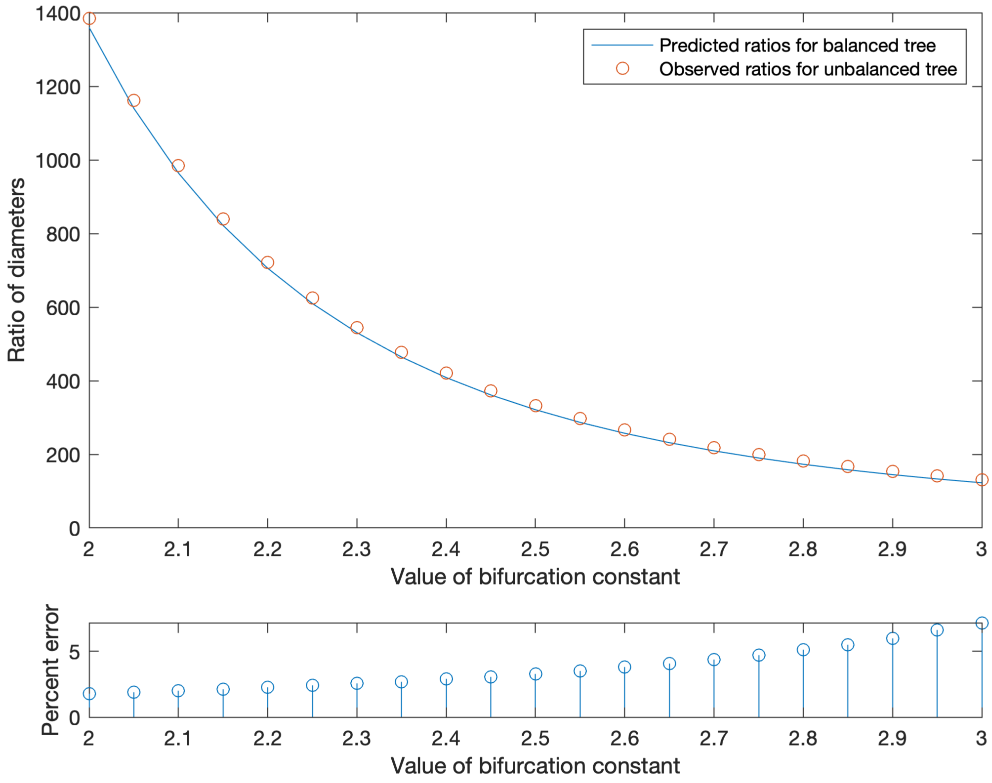

Figure 3.2: (top) Ratio of PHA diameter over average THA diameter as a function of the bifurcation constant for a balanced binary tree and for several tree realizations built in this work. (bottom) Error percentages between predicted and observed ratios of diameters. The percent difference between the ratio predicted using a balanced binary tree is less than 8%.

cant effect on the relationship between flow, pressure, and the THA diameters. It was thus possible to directly calculate the flow required to produce a tree matching the desired average THA diameter.

Figure 3.5 illustrates the growth of the vessel tree from the initial hepatic artery segmentation to the full-grown tree with $\gamma = 2.428$, $Q = 75\,\mathrm{mL/min}$, and $\Delta P = 73\,\mathrm{mmHg}$. At each cycle, the pressure, flow, and diameters were optimized as described above to create a realistic tree whose vessels taper with successive generations and for which blood flows with minimal drag. The generated tree had a PHA diameter of $4.63\,\mathrm{mm}$ and a mean THA diameter of $11.79\,\mu\mathrm{m}$ with a standard deviation of $2.45\,\mu\mathrm{m}$.

After sphere distribution, a volume image with $2\,\mathrm{mm}$ pixel widths was generated. That image was then convolved with a 3-dimensional Gaussian filter with FWHM $8\,\mathrm{mm}$ to create an image with resolution similar to that of ^{90}Y PET. A single coronal slice from near the center of the volume was extracted and is displayed as figure 3.6.

A very small percentage of particles arrived in the THAs for any average THA diameter tested in this work. Trees with $75\,\mathrm{mL/min}$ total flow and $11.8\,\mu\mathrm{m}$ average THA diameter trapped 0.087% of infused microspheres. For trees with $241\,\mathrm{mL/min}$ flow and $15.8\,\mu\mathrm{m}$ diameters, the percentage increased to 0.103%. Trees with $433\,\mathrm{mL/min}$ flow and $18.3\,\mu\mathrm{m}$ average THA diameters had 0.116% of microspheres trapped in THAs.

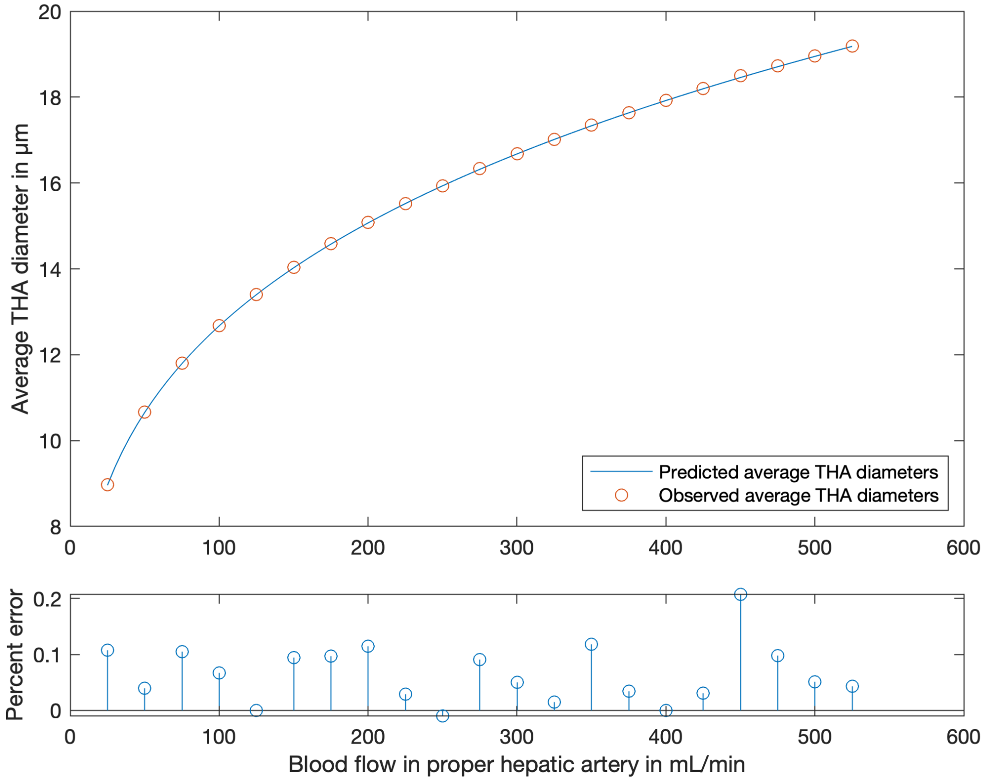

Figure 3.3: (top) Average THA diameter as a function of the total hepatic arterial flow for trees generated with pressure difference 73 mmHg and $\gamma = 2.428$. (bottom) Error percentages between predicted and observed THA diameters.

3.4 Discussion

The relatively small errors between the predicted and observed VDRs indicates that, at least for minimum drag bifurcation point optimization, the bifurcation constant can be estimated without knowing *a priori* how the tree will grow, or even how asymmetrical it will be. Furthermore, we investigated the effect of modeling a different number of portal tracts on the value of γ needed to produce

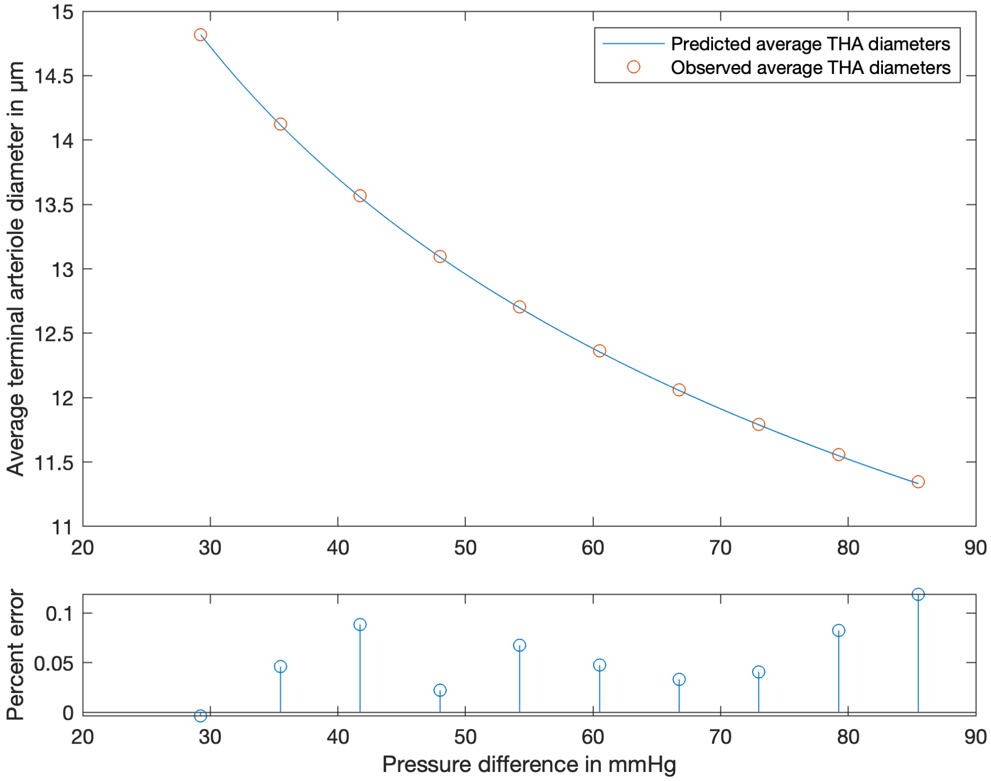

Figure 3.4: (top) Average terminal vessel diameter as a function of the pressure difference between the PHA and THAs for $75\,\mathrm{mL}/\min$ and $\gamma = 2.428$. (bottom) Error percentages between predicted and observed THA diameters.

the desired THA diameter. We found that if each portal tract contains 2.4 THAs on average (as noted by Crawford [21]), a value $\gamma = 2.57$ was calculated, which is very close to the value measured in the coronary arteries of canines and that minimizes reflection at bifurcations with equal child flow [65].

Figures 3.3 and 3.4 show that (3.7) is a reasonable method to choose a value for flow or pressure difference that will produce a tree with the desired THA or PHA diameters. Together with Kretowski's original algorithm, this allows

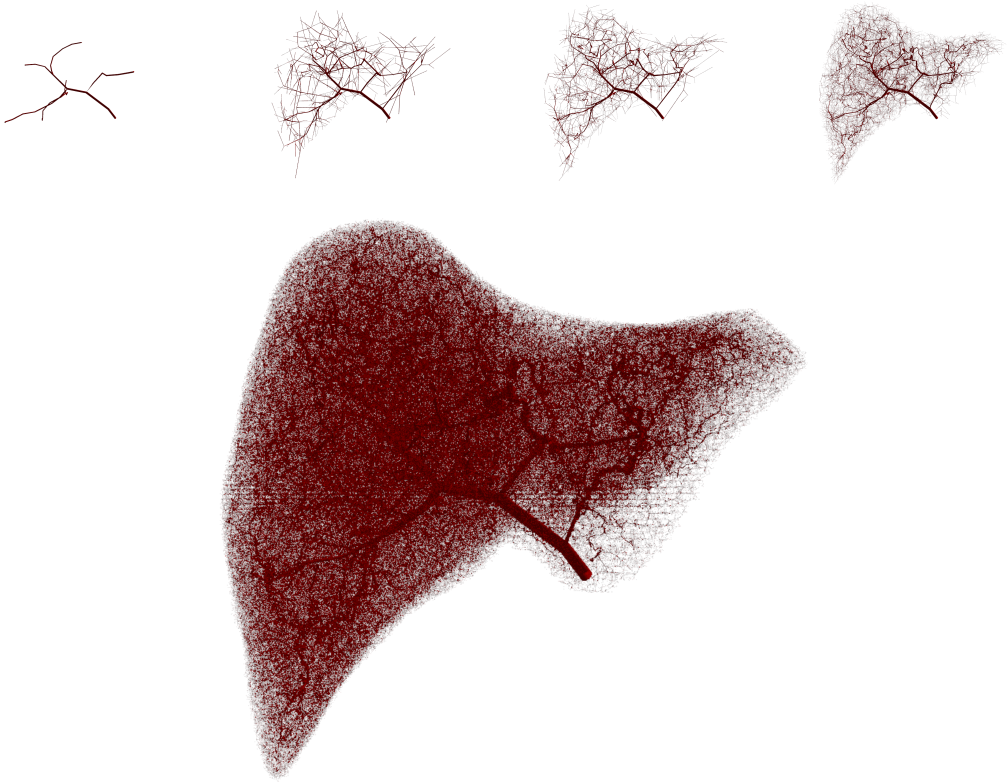

Figure 3.5: Tree growth from initial segmentation (top left), to cycle 4 (top center left), cycle 8 (top center right), cycle 12 (top right), and cycle 15 (bottom), which is the finished tree. Note that to aid visualization, the tree in earlier cycles has been scaled such that the liver shape occupies the same area of each image. Of interest is how the vessels taper in a manner comparable to true vessels. This allows embolic effects to be modeled in simulations of particle infusions.

each generated tree to be customized with respect to the different parameters of interest such as pressure difference, blood flow volume, and average THA diameter.

In this work, we adjusted flow to produce terminal vessels with an average diameter matching literature values. However, the flow required for correct diameters, $75\,\mathrm{mL/min}$, is lower than values reported in literature [57, 66]. If

Figure 3.6: A coronal slice from a simulated 120 Gy, whole-liver infusion convolved with a Gaussian filter at PET resolution. The texture is similar to that shown in Walrand *et al.* and indicates a heterogeneous distribution of spheres that may be sparing of normal tissue [10].

a Gaussian curve is representative of the data collected by Carlisle *et al.* [66], hepatic arterial flow of 75 mL/min or less would be representative of less than 3% of subjects measured. As our interest was in producing trees with reasonable THA diameters, we decided to use this value of flow. Further refinements to the flow model may help correct this apparent discrepancy, e.g., by modeling blood as a non-Newtonian fluid [52] or determining the value of the bifurcation constant at each junction in a more sophisticated manner.

The standard deviation of the generated THA diameters was only half as large as that reported by Crawford [21]. This resulted in many fewer terminal arterioles larger than 25 µm than was reported in that work. The simulations with larger THA diameters, despite having physically realistic values for flow and percentage of THAs with diameter greater than 25 µm, resulted in only slightly more particles being trapped in THAs. This is potentially important for predicting toxicity as the lobules contain physiologically important and radiosensitive structures critical for liver function [30], and microspheres trapped closer to them would deposit more dose in them. Nevertheless, the data show that the differences in the fraction of spheres trapped in THAs was less than 0.03% for the range of THA diameters investigated. The fact that so few spheres were trapped in THAs may be important as sphere trapping heterogeneity directly affects dose heterogeneity [11, 30] and may affect both tumor dose and toxicity to normal tissue.

Figure 3.6 shows a simulated PET image slice that would be obtained using an activity distribution generated using the models developed in this work. The non-uniform texture of the slice is qualitatively similar to the texture observed in patient images and those simulated by Walrand *et al*.

One potential application of the proposed method is the use of the diameter-aware particle trapping model described in this work to compare infusions of particles of different sizes. For example, the average diameter and standard deviation of MAA particles are both larger than the same parameters for glass microspheres; differences in microsphere versus MAA distribution could be used to improve the accuracy of RE treatment plans based on measured MAA activity distributions.

The particle trapping model described here allows vessels to fill with particles and may cause them to divert to other branches or trap in a parent vessel. This yields more complex clusters than an algorithm that traps all particles in terminal arterioles, as was assumed in Walrand's original work [10]. A possible method to validate the proposed particle trapping model is to perform cluster analysis on the particle distribution and compare that with clusters observed in actual treated liver tissue. As clustering behavior may be very important to normal liver dose tolerance [30], producing realistic deposition patterns could allow trees generated using this method to be used in treatment planning. Activity distributions resulting from realistic clusters of spheres can also be used to test and validate image reconstruction methods targeting improved estimation of RE activity images.

Another potential improvement to this model is modifying the macrocells to represent hypervascularized and necrotic tissue in addition to normal parenchyma. Simulations with such tissue heterogeneity may capture important information about the tumor dose and normal tissue toxicity.

This model has potential applications in patient-specific treatment planning. In particular, the model of hepatic arterial vasculature can be made patient specific using imaging data in at least three ways. First, it can easily be adapted to the shape of the liver of a specific patient, obtained, e.g., from a CT image. Second, the initial vascular tree used to seed the vessel growth algorithm could be obtained from high resolution CT or MR angiography images. Finally, perfusion patterns measured via MR or CT imaging or flow or pressure measurements made using the catheter could potentially be used to constrain these parameters in the images. All of these together could provide a patient-specific model of the vasculature and, when combined with a model of particle trapping, be used to estimate dose distributions at a microscopic level. Combined with radiobiological models [11], this could provide patient-specific estimates of liver toxicity.

3.5 Summary

In this work, we have presented a new method for generating realistic models of the hepatic arterial tree using a macrocell growth technique. The generated tree conserves mass, satisfies Murray's law of vessel diameters at bifurcation points, and uses Poiseuille's law to calculate the pressure change through the vascular network. Physical parameters describing blood flow through the tree were based on literature values and modified to provide realistic average diameters for the terminal hepatic arterioles. A model for trapping particles with a known distribution of diameters was developed. The combination of these methods is useful for generating realistic activity distributions to validate image reconstruction methods and to explore the effect of various parameters, including differences in particle diameter distribution, on the microscopic dose distribution. The method allows for specification of the initial hepatic arterial tree, patient volume, and local variations in blood flow, providing future potential for improved patient-specific treatment planning.

Chapter 4

Verification of a Method to Detect Glass Microspheres via Micro-CT

4.1 Introduction

Yttrium-90 (^{90}Y) RE is a widely-used treatment for unresectable liver cancer involving the administration of radioactive, embolic microspheres into the hepatic artery. RE has an advantage over conventional external beam radiation therapy because the average dose delivered to liver tissues can be significantly higher [11, 19] with minimal toxicity to uninvolved hepatic parenchyma. However, advancing treatment planning methods in RE requires a greater understanding of how microspheres deposit in normal and tumor tissues, as microscopic analysis has shown that microspheres trap in clusters during the infusion process [67]. This heterogeneous distribution of microspheres is believed to be crucial in explaining the observed normal-tissue-sparing effect [8] and the high tumor doses [67]. Complete three-dimensional (3D) characterization of microsphere distributions within tissue samples could enable microscale dose analysis of the tissues and comparison of the calculated doses with histological analyses of tissue samples to find correlated tissue effects. Additionally, several authors have proposed methods for generating models of liver vascular anatomy and simulating the transport and trapping of microspheres [10, 11, 15, 68]. Walrand *et al.* have specifically described a radiobiologic model that considers both microsphere clustering and tissue structure to predict the risk of toxicity in liver tissue [11]. The accuracy of those models depends on how realistically glass microsphere clustering is simulated, and a small-scale analysis of microsphere distributions in tissue would provide data to validate those models.

Traditional methods to determine microsphere locations are manual and labor- and time-intensive processes that involve dividing small sections of liver into many thin slices (∼5-200 µm), staining them, taking optical micrographs, and noting the two-dimensional locations of microspheres [43, 67, 69–72]. In the literature, analyses of only small regions using this method have typically been reported [43, 67, 71, 72], likely due to the effort involved in preparation and scanning. Further, sphere locations and cluster sizes can typically be characterized in only two dimensions, due to the complexity and extreme care necessary to collect spatially comparable data from consecutive slices thin enough to be visualized under light microscopy [43]. The FDA has approved two varieties of microspheres to treat liver cancers, SIR-Spheres (SIRTEX Medical Limited), a polymer-resin microsphere that has been labeled with ^{90}Y with mean diameter of about 32 µm, and TheraSphere (Biocompatibles UK Limited) an yttrium-doped borosilicate glass microsphere with mean diameter of about 25 µm [69]. While the typical process of sectioning tissue via microtome is able to slice polymer-based microspheres without sphere motion [43], its effect on glass microsphere locations, whether due to the blade dragging spheres downward during slicing or by moving microspheres in a direction normal to the plane of the slice, has not been reported.

This work describes and verifies a method to estimate the quantities and three-dimensional locations of glass microspheres in whole tissue samples using a high-resolution micro-CT scanner and an automated image analysis algorithm. This method allows microdosimetry and clustering behavior evaluation in large sections of *ex-vivo* tissue without requiring the involved, time-consuming tissue sectioning and scanning process.

4.2 Materials and methods

Use of patient data included in this manuscript was approved by the Johns Hopkins Hospital Institutional Review Board.

The process of analyzing micro-CT images to detect and localize ^{90}Y glass microspheres occurs over three stages. Stage I takes advantage of the large difference between the attenuation coefficients of the microspheres and the background medium (e.g., liver tissue) by using intensity thresholding to detect regions that contain microspheres. Stage II, sphere quantification, estimates the number of microspheres in each detected region using the voxel values in that region. Stage III, sphere localization, uses both the detected regions and the estimated sphere quantities in each region to estimate a three-dimensional location for each microsphere. Degrading factors inherent in CT images, such as noise due to the probabilistic nature of x-ray beam transmission and detection, system blurring due to geometric properties of the CT system, photon scatter and penetration during imaging, and other artifacts such as beam hardening or rings, require parameter choices to be coordinated between stages to mitigate their effects and produce the best overall detection and localization results. Detection and localization algorithm performance was measured using a phantom with embedded microspheres that could be scanned both optically and via micro-CT. The utility of the algorithm was then demonstrated by processing a human tissue sample.

4.2.1 Phantom preparation and imaging

Phantoms that could be scanned via micro-CT and verified using an independent modality were generated to characterize the performance of the algorithm for this system. Following the basic approach described by Marxen *et al.* [47], the phantoms were generated by sandwiching an agar/microsphere solution between plastic coverslips. Those coverslips were sealed and fixed to thin, optically transparent plastic sheets using a toluene-based mounting medium. The phantoms were placed on a microscope slide only for transmission light microscope scanning, shown in figure 4.1a; during CT scanning the slide was not present, as would be the case for scanning tissue samples, to avoid the influence of the highly attenuating microscope slide on boundary regions. Optical micrographs of the phantoms were taken with a pixel size of $2.2\,\mu\mathrm{m}$ in 96 separate images that were stitched into a larger composite image using phase correlation and simple image translation. Two-dimensional microsphere center locations were then recorded manually.

Sixteen hours after the phantoms were created and optically scanned, they were gently stacked between Styrofoam slabs, wrapped in Parafilm, and scanned using a SkyScan 1176 micro-CT scanner to detect the embedded microspheres, as shown in figure 4.1b. A total of 656 high-resolution projections spaced 0.3

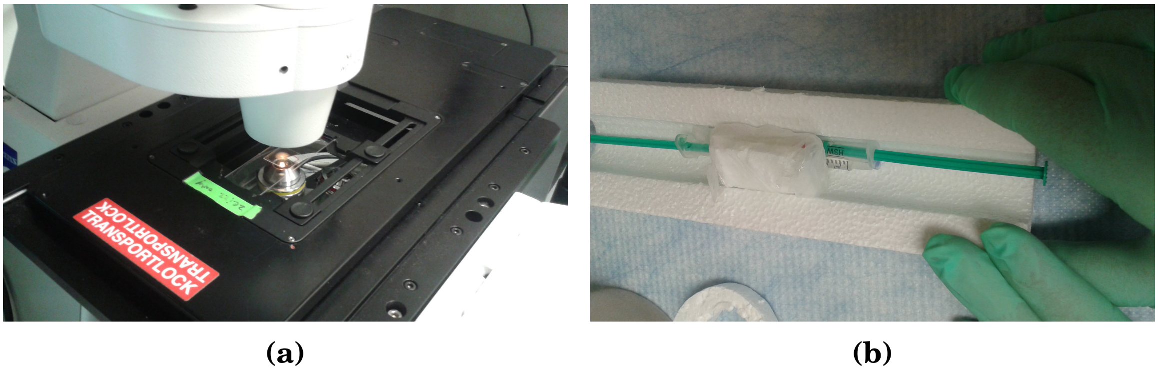

(a) (b)

Figure 4.1: (a) Each phantom was scanned via transmission light microscopy and two-dimensional microsphere locations found in the micrograph were recorded. (b) To prepare the phantoms for micro-CT scanning, several phantoms were gently stacked between Styrofoam pieces and wrapped in Parafilm. That package was placed above phantoms filled with water and formalin that were scanned to allow the CT image voxels to be transformed into Hounsfield units (HU).

degrees apart with a projection bin size of 8.74 µm were taken of the phantoms. The tube voltage was set to 90 kVp for the scans and each projection was collected twice, resulting in a total exposure of 0.695 mA s for each projection angle. To mitigate the negative effects of beam hardening on detection performance, both copper and aluminum filters were used. The resulting projections were reconstructed using NRecon (SkyScan) 1.7.3, to produce images with 8.74 µm voxels. Software-based beam-hardening correction was disabled due to erratic effects on quantification, but ring artifact and interior reconstruction corrections were enabled to improve scan uniformity.

4.2.2 Detection and localization algorithm development and verification

4.2.2.1 Stage I: Region detection

The first step in detecting regions containing microspheres was to choose an intensity threshold between the attenuation coefficient of the background and the microspheres. Noise in the reconstructed images could cause background voxels to exceed the detection threshold and appear as spurious detected regions. In high-resolution scans where one microsphere occupied many contiguous voxels, such spurious regions could be ignored by detecting and removing the smallest connected components of the image via area filtering with 26-connectivity [73], represented as Ψ_{area} below. Groups of connected voxels whose values exceeded the detection threshold are referred to as detected sub-regions in this work. Noise could cause variations in the voxel values of the sub-regions, and partial volume effects due to blurring could spread sub-region voxel intensities into neighboring voxels. Thus, considering the lower-intensity neighboring voxels in addition to the voxels in the detected sub-regions was used to mitigate the impact of these effects on later stages. This was achieved by dilating those sub-regions into full regions by a spherical structuring element, B, with radius d_r [74]. The result of the region detection stage was represented as the connected components of $I_{R_{all}}$, the binary image marking all detected regions described by

$$I_{R_{all}} = \Psi_{area}(I > t, n) \oplus B \tag{4.1}$$

where I is the CT image, t is the detection threshold, and n is the minimum sub-region volume. The choices of these parameters affected not only the accuracy of region detection, but also subsequent stages. For example, the threshold and minimum volume were chosen with consideration for both the number of spurious regions and erroneously omitted regions that resulted. However, as parameter choices affected not only the accuracy of region detection but all later stages, optimal choices of these parameters also depended on the capabilities and deficiencies of those stages.

4.2.2.2 Stage II: Microsphere quantification

After finding the CT image regions containing microspheres, the next stage was estimating the number of microspheres in each region. This was accomplished by considering the integrated intensity in an arbitrary region R of the CT image:

$$I_R = \sum_i \sum_j \sum_k \mathbf{1}_R(i,j,k) \cdot \mu(i,j,k) \tag{4.2}$$

where I_R is the integrated intensity of region R, $\mathbf{1}_R$ is the indicator function of the region and $\mu(\cdot)$ is the linear attenuation coefficient at each location in the image. Real tissue contains inhomogeneities, but as the attenuation coefficient of the microspheres was both uniform and much higher than the background, it was possible to ignore those inhomogeneities and treat the system as if it were composed of two uniformly attenuating media: background and microsphere. Then, I_R can be written as the volume-weighted sum of the background and microsphere attenuation coefficients,

$$I_R = \frac{v_{sphs}}{v_{vox}} \mu_{sph} + \frac{v_R - v_{sphs}}{v_{vox}} \mu_{bg}, \tag{4.3}$$

where v_{vox} is the volume of a voxel, v_{sphs} is the combined volume of all spheres in the region, v_R is the volume of the region, and μ_{bg} and μ_{sph} are the attenuation coefficients of the background and microspheres, respectively. Assuming the region contains the full volume of each microsphere, the volume of all spheres in R can be expressed in terms of individual spheres. Substituting into (4.3) gives

$$I_R = \frac{\sum_i^n v_{sph_i}}{v_{vox}} \mu_{sph} + \frac{v_R - \sum_i^n v_{sph_i}}{v_{vox}} \mu_{bg} \tag{4.4}$$

where v_{sph_i} is the volume of microsphere i, and n is the number of microspheres in the region. If spheres in region R are assumed to all have diameters of 25 µm then the total estimated volume is $v_{sphs} \approx n \cdot v_{sph}$, where v_{sph} is the volume of the average microsphere. If the number of spheres in region R is high, then the approximation for v_{sphs} is likely to be more accurate, as variations in sphere volume would tend to average out. For smaller regions, there is a greater chance of misestimating the integrated intensity of that region.

With that assumption, equation (4.4) can be rewritten as

$$I_R = \frac{n \cdot v_{sph}}{v_{vox}} \mu_{sph} + \frac{v_R - n \cdot v_{sph}}{v_{vox}} \mu_{bg} \tag{4.5}$$

A further assumption is that the region detection method produces regions whose volumes scale linearly with the number of spheres contained in them (i.e. $m \cdot v_{R_n} = n \cdot v_{R_m}$, where v_{R_m} and v_{R_n} are the volumes of regions containing m and n microspheres, respectively). Then

$$I_R = n \left(\frac{v_{sph}}{v_{vox}} \mu_{sph} + \frac{v_{R_1} - v_{sph}}{v_{vox}} \mu_{bg} \right) = n \cdot \zeta, \tag{4.6}$$

where v_{R_1} is the detected volume of a region with a single, average-size microsphere. The method, referred to as with-background (WBG), described in equation (4.6), estimates that the number of spheres in region R by calculating the integrated intensity of the region and dividing by a scalar factor, ζ.

However, the assumption that the volume of a region containing many spheres is proportional the volume of a single-sphere region is only true for an ideal system. With system blurring, the size of a detected region depends not only on the threshold chosen, but on the relative microsphere positions within the detected region volume. It is possible to reduce the influence of the region volume on quantification by rewriting (4.5) as

$$\hat{I_R} = I_R - \frac{v_R}{v_{vox}}\mu_{bg} = n\frac{v_{sph}}{v_{vox}}\left(\mu_{sph} - \mu_{bg}\right) = n \cdot \hat{\zeta} \tag{4.7}$$

where $\hat{I_R}$ is the integrated intensity of the region above the background attenuation coefficient, and $\hat{\zeta}$ is the corresponding scalar factor relating the number of spheres in a region to the intensity over background.

Equation (4.7), referred to in this work as the no-background (NBG) method, eliminates assumptions about the relationship between the number of contained microspheres and total region volume but retains much of the simplicity of the WBG method.

Image degrading factors could also contribute to errors in sphere quantification. Both the WBG and NBG methods could be affected by noise within the regions, as it could increase or decrease the measured attenuation coefficients of the contained voxels. This, in turn, could result in over- or underestimation of the number of spheres in those regions. Sphere quantification accuracy could also be impacted when system blurring caused intensity from microspheres in a region to extend beyond the detected region boundaries, resulting in quantification considering only some of the voxels affected by microsphere intensities. If the regions considered for microsphere quantification were dilated by an appropriate value of d_r, then both degradation issues could be mitigated. Given an appropriate dilation radius, the integrated intensities of larger regions should exhibit less deviation than undilated regions, and all voxels influenced by microsphere intensities will have been included in each region. The accuracy of the NBG method should not be overly sensitive to the choice of d_r, provided it is large enough to mitigate the errors described above. However, the WBG method is expected to be much more sensitive to the choice of d_r, as it would affect the accuracy of the assumption that region volumes scale linearly with the number of microspheres contained in them. Therefore, the optimal dilation radius during region detection should depend on the quantification method to be used. This exemplifies the fact that optimal quantification could require adjustments to region detection parameters.

As another example, if degrading factors caused spurious regions in the first stage, it would seem reasonable to adjust the detection threshold to minimize the total number of spurious and incorrectly omitted regions. However, because both methods used for the sphere quantification stage were capable of determining when regions had no microspheres, and were thus spurious, they could not detect spheres in regions omitted in stage I. Thus, minimizing the number of incorrectly omitted regions is, for these quantification methods, more important than minimizing the number of spurious regions.

4.2.2.3 Stage III: Microsphere localization

The final stage uses the microsphere quantities estimated in stage II and the detected sub-regions found in stage I to estimate locations for each detected microsphere. As with the previous two stages, localization could be impacted by image degrading factors, such as noise, which could cause bright points in areas where there were no actual microspheres, and system blurring, which could cause microsphere peaks to lose sharpness or even merge. There are a variety of potential methods to estimate microsphere locations from the detected regions and estimated sphere quantities. If localization were relatively less important than quantification, then assuming the microspheres were distributed proportionally among the voxels of the detected sub-regions would have been sufficient. However, as described above, the proposed method was developed in order to accurately analyze the micro-dose deposition of ^{90}Y emitters. The sharp peaking of the ^{90}Y dose kernel means that incorrectly localized microspheres could have a significant impact on the dose distribution error. Thus, accurate, discrete microsphere location estimation would likely result in substantially increased dose distribution estimation accuracy. The simplest method investigated for estimating a discrete location assumed that all n microspheres detected in a region were co-located at the region's centroid. Similar to the proportional-distribution method above, this could produce in-accurate dose maps where an excessively high dose was estimated for the centroid voxel, and insufficient dose was estimated for all surrounding voxels. A more realistic method was to place the n microspheres at the n largest local maxima of the sub-region voxels. This would partially address the issue with co-locating microspheres, but localization inaccuracies would remain due to noise in the sub-regions and blurring between microsphere peaks. If those errors were mostly due to microsphere location estimates being unrealistically close together, then a refinement would be to select the n largest local maxima subject to the constraint that sphere center locations were separated by the average microsphere diameter. This method, referred to in this work as well-spaced local maxima, potentially suffers from errors due to non-uniform microsphere sizes and noise in the sub-regions. Another investigated approach used voxel-weighted k-means cluster analysis to identify n distinct partitions within the detected sub-regions and stored the centroids of each cluster as the localized microsphere centers. Using clustering should avoid issues with co-located microspheres and mitigate issues with noise, assuming the voxel values in a sub-region are more heavily affected by microsphere intensities than noise. However, this clustering method could still suffer from typical k-means issues, such as producing different results in different runs, or converging to a local minimum.

4.2.3 Algorithm verification

To compare the micro-CT scans to the optical micrographs, a maximum-intensity projection (MIP) of the CT image was created along the vector normal to the plane of microspheres. A projective mapping was then estimated between the CT MIP and the optical micrograph using common features visually identified in the two images. Region detection was performed on the full CT image, and those three-dimensional regions were projected to a plane along the same vector. In the rare case that two regions overlapped along that axis, the larger region was chosen to occupy the shared area of the resulting two-dimensional image. The microsphere locations, marked in the phantom, were projected into the MIP image space of the micro-CT and each was assigned to the region overlapping it, if any. Peripheral regions of the phantom that showed obvious shifting due to agar desiccation were excluded.

Optimal parameters for the detection and quantification methods, including least-squares estimates of ζ and $\hat{\zeta}$, were determined using the integrated intensity, the integrated intensity above background, and the true number of microspheres within each detected region of one phantom. A different phantom was then processed, using the parameters estimated from the first phantom in the analysis, to estimate microsphere locations using the methods described above.

4.2.4 Performance evaluation

For each stage of the algorithm, different metrics best characterized performance. For region detection, the optimal thresholds, minimum sub-region volumes, and dilation radii could be approximated by testing a range of values and determining the percentage of microspheres contained within regions and the percentage of regions that actually contained spheres. Best performance for this stage minimized the number of spurious regions without incorrectly decreasing the number of microspheres detected.

After detecting potential regions containing spheres, the number of spheres in each region was estimated using the WBG and NBG quantification methods. The mode of the voxels outside of regions in the same plane as the microspheres was used as the background attenuation coefficient. Overall stage performance was evaluated by first considering each region individually, then aggregating the region performance data for the whole phantom. Specifically, for each region the number of microspheres was estimated and compared to the true number observed in the optical micrograph, and the number of true positives (TPs), false negatives (FNs), and false positives (FPs) were recorded. As an example, if a region contained M microspheres but the number estimated was $M+N$, then M TPs and N FPs were recorded. Conversely, if the number estimated was $M-N$, then $M-N$ TPs and N FNs were recorded. Performance for the whole phantom was reported by aggregating those results to calculate the true positive fraction (TPF), the number of TPs divided by the total number of spheres, and false positive fraction (FPF), the number of FPs divided by the total number of spheres [47]. Optimal choices for the algorithm parameters were those that maximized the difference between the TPF and FPF. The impact of changes in the region detection parameter on the performance of the sphere-quantification stage was evaluated by testing the same parameter ranges as in region detection and examining the resulting TPF and FPF.

Because ζ and $\hat{\zeta}$ were found using least-squares estimation, it is possible that larger, more attenuating regions would have an outsized influence on the final estimates of these parameters. To allay those concerns, 10,000 estimates of ζ and $\hat{\zeta}$ were found using bootstrapping, and the 95% confidence intervals of the TPF and FPF were examined. The 95% confidence interval for the total number of estimated microspheres was also calculated to check the accuracy of this method for estimating the total dose to a scanned region.

Radiation absorbed-dose maps were created by convolving a dose-voxel kernel (DVK) with a 3D time-integrated activity map formed using the estimated microsphere locations. The DVK was calculated for $72\,\mu\text{m}$ voxels using MCNP-6 (Monte-Carlo N-Particle, Los Alamos National Laboratory, Los Alamos, NM) [75] with the ^{90}Y beta spectrum defined by Eckerman [76] in a 5x5x5 cm block of liver tissue [77]. An electron/photon-coupled transport simulation of primary and secondary particles was performed with an energy cutoff of 1 keV and a reduced electron step-size to limit inaccuracies related to the condensed history approximation.

The figure of merit for stage III was chosen to be the mean absolute error (MAE) between the voxels of the true and estimated dose maps. This figure of merit provided an appropriate penalty for FNs and FPs in each region, because missing or erroneously added microspheres contributed to the error in the same manner as incorrectly located spheres. Given that the optical micrograph only provided two-dimensional sphere location data, the dose from the optically determined locations was compared to that of the three-dimensional localized points by assuming the true points were all co-planar, projecting the estimated points into that same plane and comparing the resulting dose maps.

The time-integrated activity map varied slightly based on the choice of the activity map origin relative to the microsphere coordinates due to discretization effects. Thus, the average relative MAE between the true and estimated dose maps was calculated over 100 trials with the dose maps shifted by a random amount in each dimension. The error due only to the sphere localization stage was estimated by measuring the MAE between the true dose map and a map created with location estimates found using the detected regions and the correct number of microspheres. Projecting 3D locations into a single plane could hide errors that would be present if the true 3D microsphere locations were known and used for the dose MAE. Because of this, the percent reduction in dose MAE observed when reducing dimensionality was estimated by projecting the two-dimensional microsphere locations along different vectors into a single dimension and calculating the relative dose distribution errors. Finally, the stability of microsphere locations estimated using the weighted k-means clustering algorithm was studied by performing 100 trials with different initial random seeds and evaluating the variation in dose distribution error.

This algorithm's suitability for characterizing microsphere clusters in scanned samples was evaluated by comparing the histograms of the true and estimated microsphere cluster sizes, where clusters were determined using single-linkage clustering with an inter-cluster distance cutoff of 200 µm, as done by Högberg *et al.* [51].

4.2.5 Patient specimen

To illustrate the utility of these methods, the method was applied to an archived pathology specimen from a patient with an 8x5x5 cm neuroendocrine tumor in the right hepatic lobe, treated with ^{90}Y glass microspheres 10 days after microsphere calibration. The patient received a liver transplant for cirrhotic liver failure approximately 2 years after RE, at which time the specimen was obtained. Following automated microsphere identification, microdosimetry was performed on the sample which was approximately 2x1x1 cm in size.

4.3 Results

4.3.1 Phantom preparation and imaging

A careful examination of the optical micrograph revealed 1,434 microspheres in phantom 1 and 1,697 microspheres in phantom 2. The phantoms were scanned using micro-CT imaging and an example slice is shown in figure 4.2.

4.3.2 Detection and localization algorithm development and verification

The detection and localization algorithm was applied to the three-dimensional CT image in the sequence of stages described above. Those stages are illustrated in figure 4.3 using a small area of phantom 1. Parts 4.3c-4.3e demonstrate the thresholding, area filtering, and dilation operations of region detection, parts 4.3f-4.3g exemplify the estimation of microsphere quantities during the sphere quantification stage, and 4.3h shows circles estimated during the localization stage overlaying the true microsphere locations.

Due to clear shifting of the agar and microspheres near the phantom edges due to agar desiccation and gravity effects in the hours before and during the CT scan, spheres and detected regions located in the periphery of the phantom were excluded, as shown in figure 4.4, to allow the algorithm performance to be

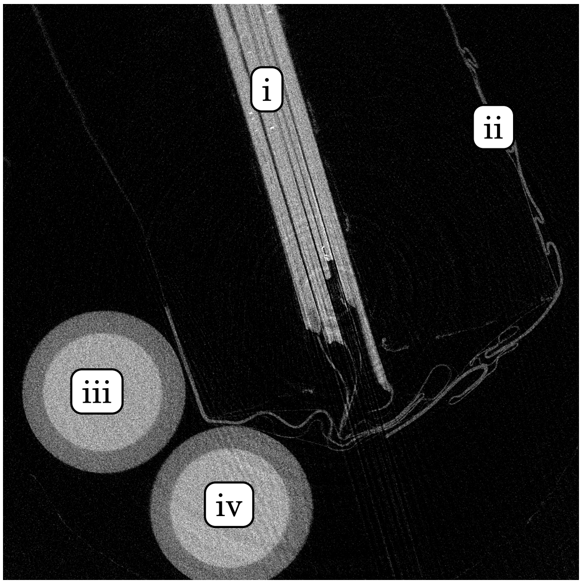

Figure 4.2: A single slice of the phantom CT scan showing (i) several stacked phantoms, (ii) the Parafilm wrapping, (iii) a small syringe filled with formalin, (iv) and a small syringe filled with water.

characterized independent of motion in the phantom. After excluding peripheral areas, 980 microspheres remained in phantom 1 and 1,555 microspheres remained in phantom 2 and were used to calculate the performance metrics.

4.3.3 Performance evaluation

Figure 4.5 shows the fraction of microspheres detected and the fraction of regions containing microspheres after region detection as a function of the detection threshold, dilation radius, and minimum sub-region volume. The fraction of microspheres detected remained fairly constant for a wide range of detection thresholds (dropping from 1.000 to 0.893 over the range 460 to 1700 HU above background), minimum sub-region volume (dropping from 1 to 0.990 over the

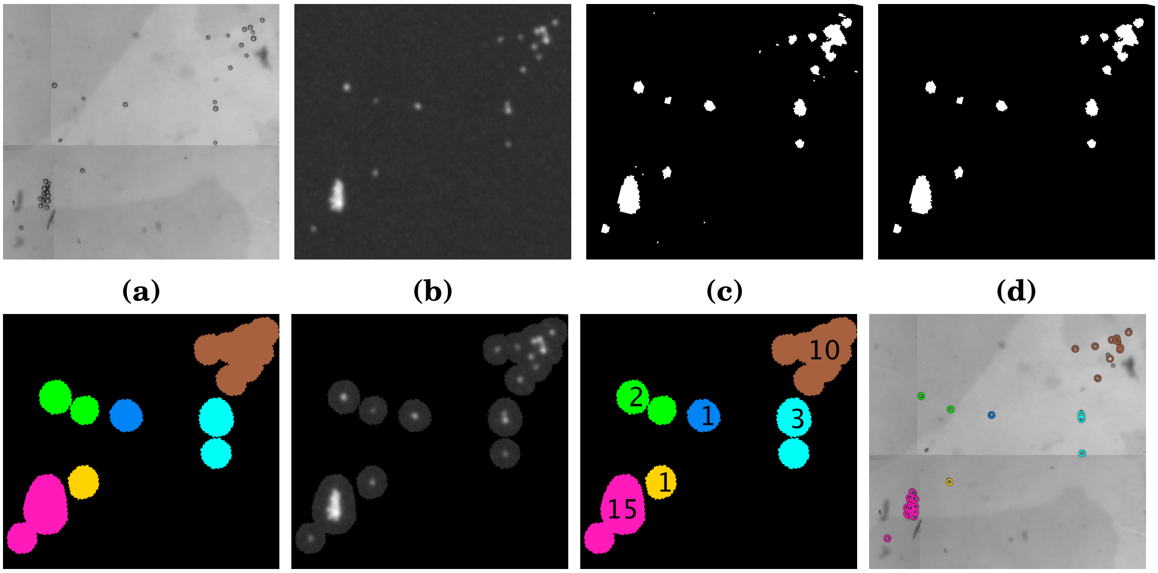

(a) (b) (c) (d)

(e) (f) (g) (h)

Figure 4.3: A visual representation of the three-stage process used to detect microspheres. (a) An optical scan of a region containing microspheres is used to determine gold-standard microsphere locations. (b) The region is scanned using micro-CT, displayed here as a MIP of the CT image. (c) Regions are detected by retaining only voxels above the detection threshold. (d) Regions much smaller than the average microsphere volume are then removed, leaving the detected sub-regions. (e) Voxels around those sub-regions are also considered during quantification. (f, g) The CT values in the regions are summed to determine the quantities of spheres present in each region. (h) Finally, localization estimates microsphere locations using the region detection and sphere quantification outputs.

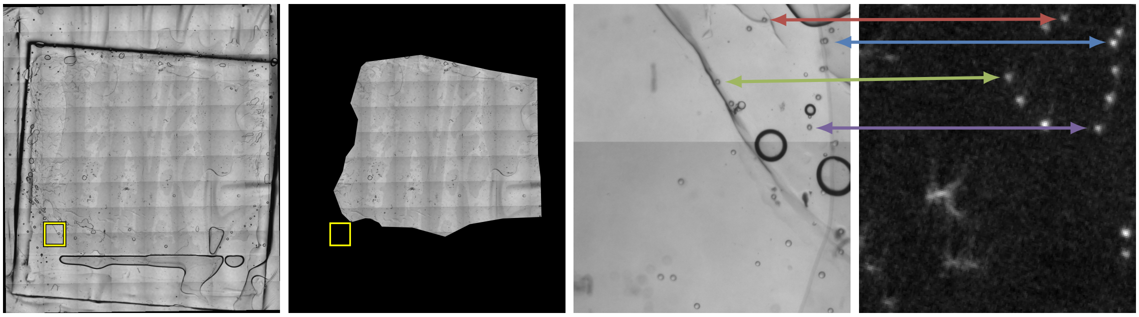
(a) (b) (c) (d)

Figure 4.4: (a) An optical micrograph of phantom 1, including areas exhibiting motion discrepancies. (b) The area of phantom 1 free from obvious motion artifacts. (c) A detailed view of an area exhibiting motion marked in parts (a) and (b). (d) MIP of the corresponding area in the longer-exposure CT image taken 16 hours later. Note that the bright areas in the top right show less evidence of motion and usually correspond to spheres in the optical image. The bottom left section contains distorted, non-compact bright regions that do not correspond to the optical image due to motion.

range 0 to 120 voxels), and dilation radii (remaining constant at 1 for radii from 0 µm to 131.2 µm). The fraction of regions containing microspheres varied more as parameters changed. Using detection thresholds below 668 HU resulted in many regions without microspheres, but fewer than 1.5% of detected regions contained no microspheres for thresholds between 668 and 1700 HU. Similarly, if no minimum sub-region volume filter was employed, thousands of spurious regions were found, but ignoring sub-regions smaller than 25 voxels reduced the number of spurious regions to 16. Increasing the dilation radius also increased the fraction of regions with spheres by merging spurious regions with nearby regions containing spheres; the fraction containing spheres was above 97.4% for the range of radii studied.

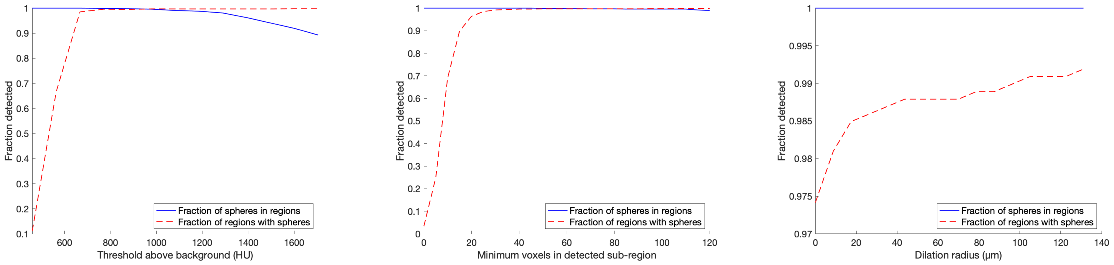

(a) **(b)** **(c)**

Figure 4.5: (a) Region detection performance as a function of threshold. (b) Performance as the minimum detected sub-region volume increased. (c) Performance as the dilation radius increased. Region detection performance was fairly consistent for large ranges of each parameter. Except when acting as the independent variable, the detection threshold was 668 HU over background, the minimum sub-region volume was 25 voxels, and the dilation radius was 17.5 µm.

Figure 4.6 shows the values of the stage II quantification metrics, the TPF, FPF, and difference between them, for both methods of sphere quantification for the same stage I parameter ranges. Results shown in the top row are for the WBG method, which assumed that region volume scaled linearly with the number of spheres present; the bottom row are for the NBG method, which did not make this assumption. The plots in figure 4.6 also show the 95% confidence interval of detection performance to illustrate the sensitivity of quantification performance to the particular regions used to estimate the number of microspheres in each region. Higher detection thresholds affected the TPF of the WBG method more strongly than it affected the TPF of the NBG method. However, because the NBG method performed best without area filtering and with large dilation radii, lower thresholds caused all microspheres to be detected in a single region, which did not permit a robust estimate of $\hat{\zeta}$. The WBG TPF peaked at 460 HU above background and dropped from 94.9% to 78.4% while the NBG TPF varied narrowly between 94.3% and 95.7% above 771 HU. The FPF of the NBG method was much higher for the lowest detection thresholds used, but for thresholds higher than 875 HU the FPFs of both methods were within 5 percentage points. The WBG method TPF performance was more consistent as the minimum volume changed, while the NBG method decreased from 88.2% to 74.8%. The FPF as the minimum volume changed remained essentially the same for both methods, neither varying more than 2 percentage points, Quantification performance was most sensitive to dilation radius. For the WBG method, the difference in TPF and FPF was maximized when including voxels within 17.5 µm of the sub-region. Including pixels beyond 17.5 µm resulted in slightly worse TPF performance and markedly worse FPF performance. Further, the 95% confidence interval of the difference between the TPF and FPF widened from 2.8% at the optimal dilation radius to 35.3% for larger radii. For the NBG method, the difference between TPF and FPF was maximized when the dilation radius was 79 µm. The 95% confidence interval for the NBG method was similar to the WBG method. The interval was approximately 3.0% at the optimal dilation radius, and for larger radii it increased to 12.5%.

The best overall performance was achieved using the WBG method with a detection threshold of 668 HU above background, a minimum sub-region vol-

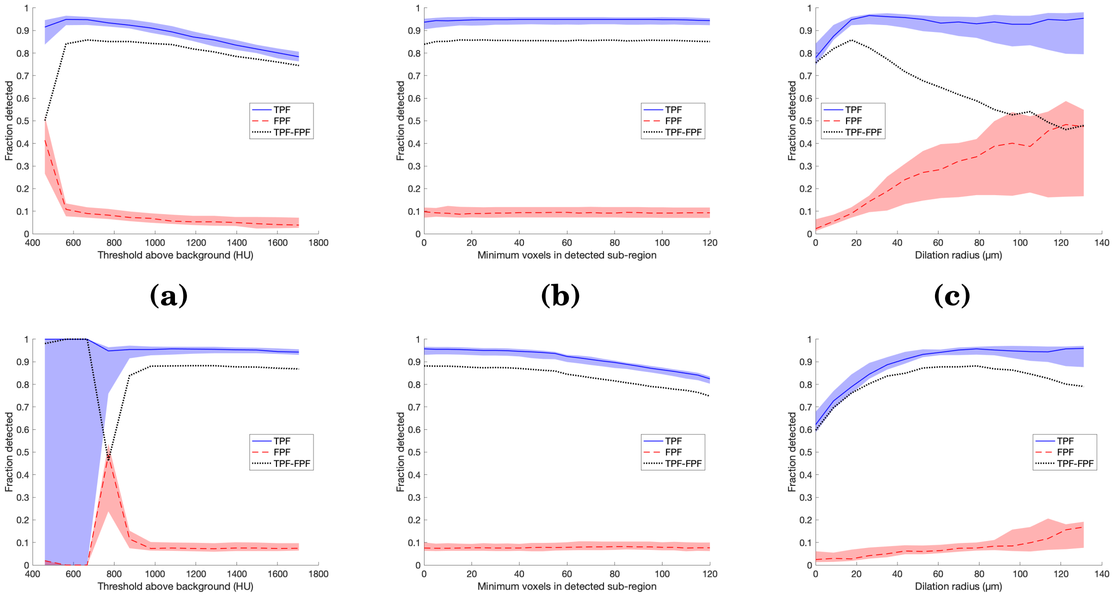

(a) **(b)** **(c)**

(d) **(e)** **(f)**

Figure 4.6: (a) (b) (c): Performance when quantifying microspheres using the WBG (region values including background) method. Unless acting as the independent variable, the detection threshold was 668 HU over background, the minimum sub-region volume was 25 voxels, and the dilation radius was 17.5 μm. (d) (e) (f): Quantification performance using the NBG (region values above background) method. Unless acting as the independent variable, the detection threshold was 1,082 HU over background, the minimum sub-region volume was 0 voxels, and the dilation radius was 78.7 μm. These default parameters were chosen to produce best results for each method. For both methods, (a) and (d) compare performance as a function of the detection threshold, (b) and (e) show performance as a function of the minimum sub-region volume, and (c) and (f) compare performance as a function of dilation radius. Quantification performance was more sensitive than region detection performance to the values chosen for each parameter. The 95% confidence intervals for each measurement are shown, illustrating the sensitivity of each method to the measurements used for estimation. The NBG performance for thresholds below 771 HU has good average performance because the low thresholds and large dilation radius produce 7 regions, 6 of which are spurious, and 1 that contains all microspheres, but more regions are necessary to estimate $\hat{\zeta}$ without over-fitting. From 771 HU to 1700 HU the number of regions detected varies between 278 and 1,668, which does allow $\hat{\zeta}$ to be estimated. Similar issues do not occur at the same threshold with the WBG method due to the smaller dilation radius.

ume of 25 voxels, and a dilation radius of 17.5 µm. In phantom 1, 464 regions were detected, of which 439 contained 980 microspheres. The quantification scalar, ζ, was estimated to be $2.8 \cdot 10^4$ HU per microsphere. Using this scalar during microsphere quantification correctly estimated that 13 of the remaining 25 regions had no microspheres. The proposed algorithm estimated that there were 1,017 microspheres in the phantom (95% confidence interval of 976 to 1056 microspheres), giving an error of 3.8% (confidence interval -0.4%-7.8%). When the parameters were applied to phantom 2, 453 regions were detected, 448 of which contained 1,553 microspheres. The proposed algorithm estimated there were 1,532 microspheres in the phantom, giving an error of 1.5%. When applied to phantom 2, the quantification stage had a TPF of 93.8% and a FPF of 4.8%.

Sphere localization was performed on the output of the WBG quantification stage applied to phantom 2 using the different localization methods described above. The relative MAE between the dose maps of the true and estimated microsphere locations, averaged over 100 trials with randomly shifted origins, is shown for each localization method in figure 4.7. Using k-means clustering on the voxels in each detected sub-region best approximated the microsphere locations, giving the lowest absolute dose distribution error of 4.2% (about 5.0 Gy for a 120 Gy treatment). The average relative MAE between the true dose and that estimated using the best localization method and the correct number of microspheres for each region had a relative error of 1.6% (about 1.9 Gy for a 120 Gy treatment) and is also shown in figure 4.7. Projecting the estimated microsphere locations into a single dimension prior to measuring the relative dose distribution error reduced the error to about 2.6% for all stages, or 0.98% when given correct microsphere quantities. The mean relative dose distribution error from 100 k-means localization trials was $4.2 \pm 0.11\%$.

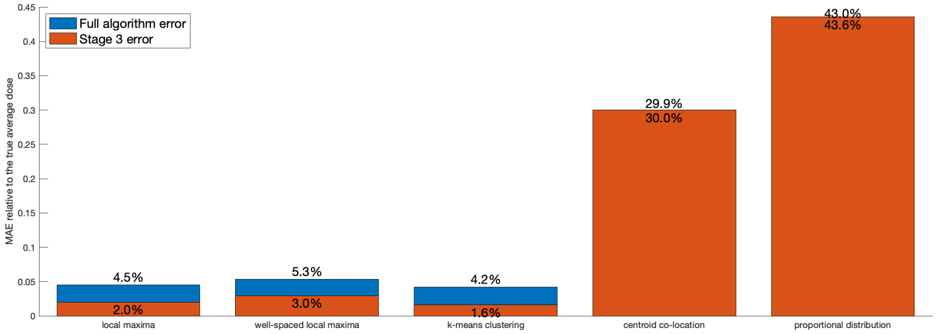

Figure 4.7: A comparison of the relative MAE of the different proposed microsphere localization methods applied to phantom 2 processed with optimal parameter values. The upper value on each bar is the MAE of the full algorithm using the regions detected in stage I and the number of microspheres estimated in stage II, and the lower value is the MAE of just the localization stage using the regions detected in stage I and the correct number of microspheres in those regions. The worst-performing localization methods performed worse when the correct number of microspheres were localized due to the likelihood of misplacing more microspheres. The more accurate methods improved when the correct microsphere counts were used. The lowest-error localization method used the centroids of the clusters detected using k-means clustering on the detected subregion voxels with weightings based on the voxel values. Most of the error for k-means-based localization was due to inaccuracies in the number of microspheres in each region.

Figure 4.8 compares the frequency of clusters of different sizes for the true microsphere locations and those estimated via the full method presented here with a bin size of 3.

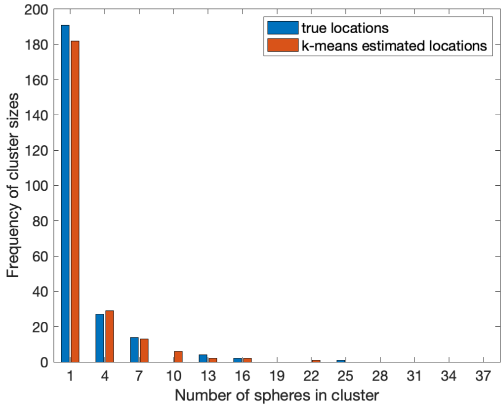

Figure 4.8: A comparison of the histograms of detected and true microsphere clusters formed via single-linkage clustering with a 200 µm inter-microsphere distance cutoff.

4.3.4 Patient specimen

A total of 7,671 microspheres were detected in the human tissue sample. The spheres aggregated into 1051 clusters (defined as groups of spheres separated by at least 200 µm). Figure 4.9 shows a visualization of the detected microspheres within the tissue sample, the corresponding dose map, and a detail view indicating that the detected microspheres organize into linear 3D patterns as the microspheres fill vessels. Figure 4.9b shows the highly heterogeneous pattern of absorbed dose deposition where 40% of this section of tumor tissue received $<$ 20 Gy (V20 = 60) while areas with dense sphere deposition received over 3000 Gy.

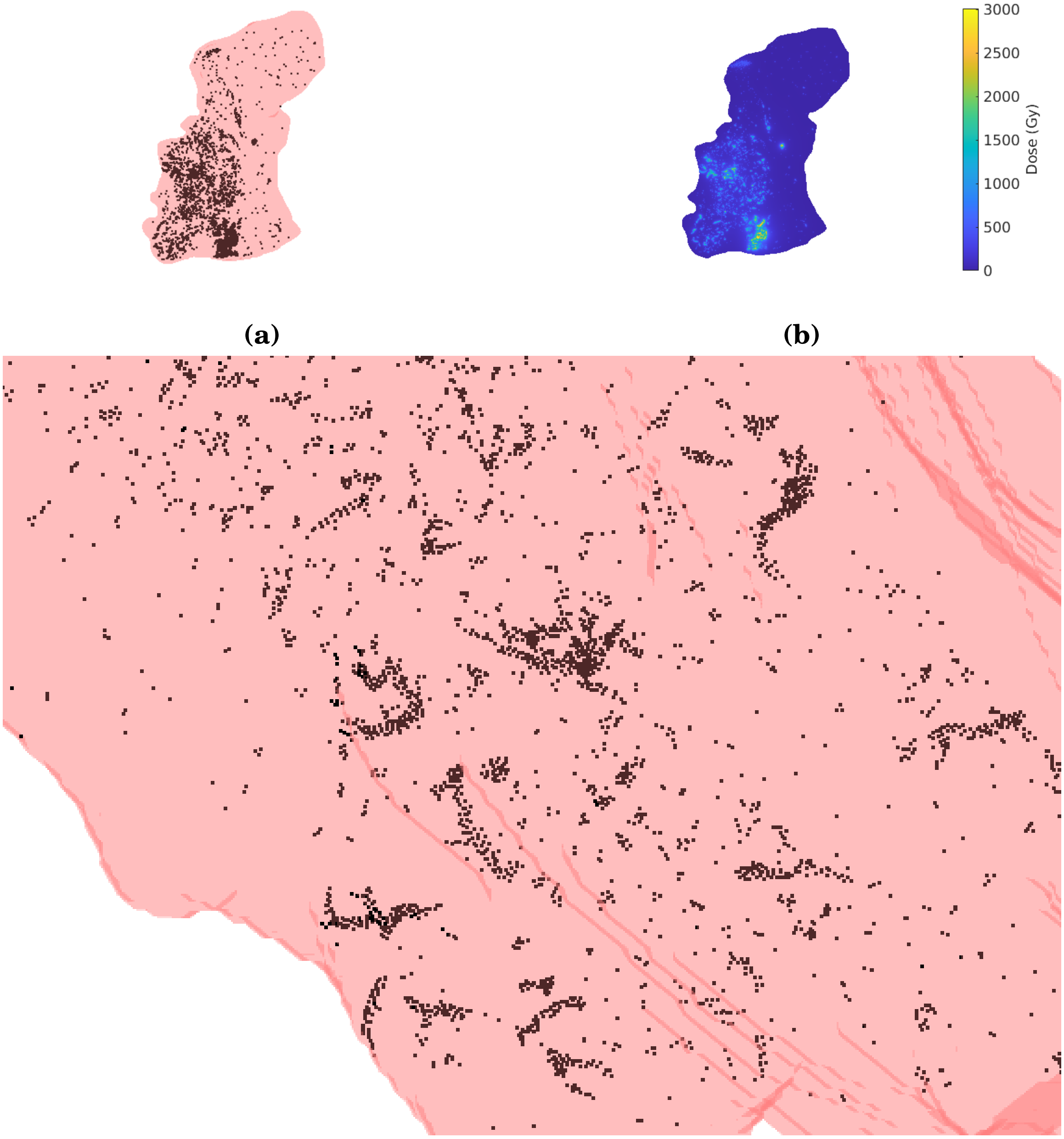

(a) **(b)**

(c)

Figure 4.9: (a) A visualization of the microspheres in a tissue sample of a neuroendocrine tumor treated with glass microspheres prior to resection. (b) A MIP of the dose map corresponding to the detected microsphere locations. (c) A detailed view of the sample center that shows the vessel-like shapes of some of the detected microsphere clusters.

4.4 Discussion

The performance of region detection was most strongly correlated with the detection threshold. Varying the minimum volume and dilation radii had only modest impacts on both the fraction of microspheres contained in regions and the fraction of regions that were spurious. The range of useful parameters was narrowed by considering the impact of region detection parameter choices on later stages.

Most of the final error in detection and localization was due to the sphere quantification stage. Figure 4.6 demonstrated that the best results were found using the WBG method with a relatively low detection threshold and a small dilation radius. Few voxels outside of those occupied by microspheres were included when a small dilation radius was used, which improved the accuracy of the approximation on which WBG depended, $v_R \approx n \cdot v_{R_1}$. Conversely, the NBG method performed best with a larger dilation radius because it didn't explicitly depend on the volume of the region. Examining fewer voxels can make the method more sensitive to noise, as the effects of noise on the integrated intensity of larger regions is more likely to balance out. The potential sensitivity of the WBG method to noise is important to consider because in a large tissue sample the noise is expected to be higher than in the thin phantoms used in this work. The WBG method is also more sensitive to artifacts that are only partially mitigated, such as the attempted ring correction shown in figure 4.10. If the voxels neighboring the detected sub-region are included in the integrated intensity then the excessively bright and dark voxels will tend to cancel out, but if the region is too small then false positive microsphere locations will be estimated.

There are some benefits to using a small dilation radius, however. If the background medium is non-uniform, a smaller dilation radius can make quantification more robust by mainly including voxels overlapping microspheres. For example, if microspheres are trapped in a tissue sample with regions of air, then both quantification and localization can be affected due to parts of the region contributing much less than expected to the integrated intensity. If very few voxels containing background are included, then the contribution of unexpected pixel values will still be small relative to the overall region sum.

Thus, while the best overall performance with these phantoms was achieved using the WBG method, the different strengths of each method merit consideration when deciding which method to use for quantification. Interestingly, Marxen *et al.* described an algorithm for sphere quantification that appears very similar to the WBG method, though they reported a higher FPF, possibly due to not being able to filter spurious regions due to similar microsphere and CT voxel sizes [47].

The MAE between the true and estimated dose maps was relatively small,

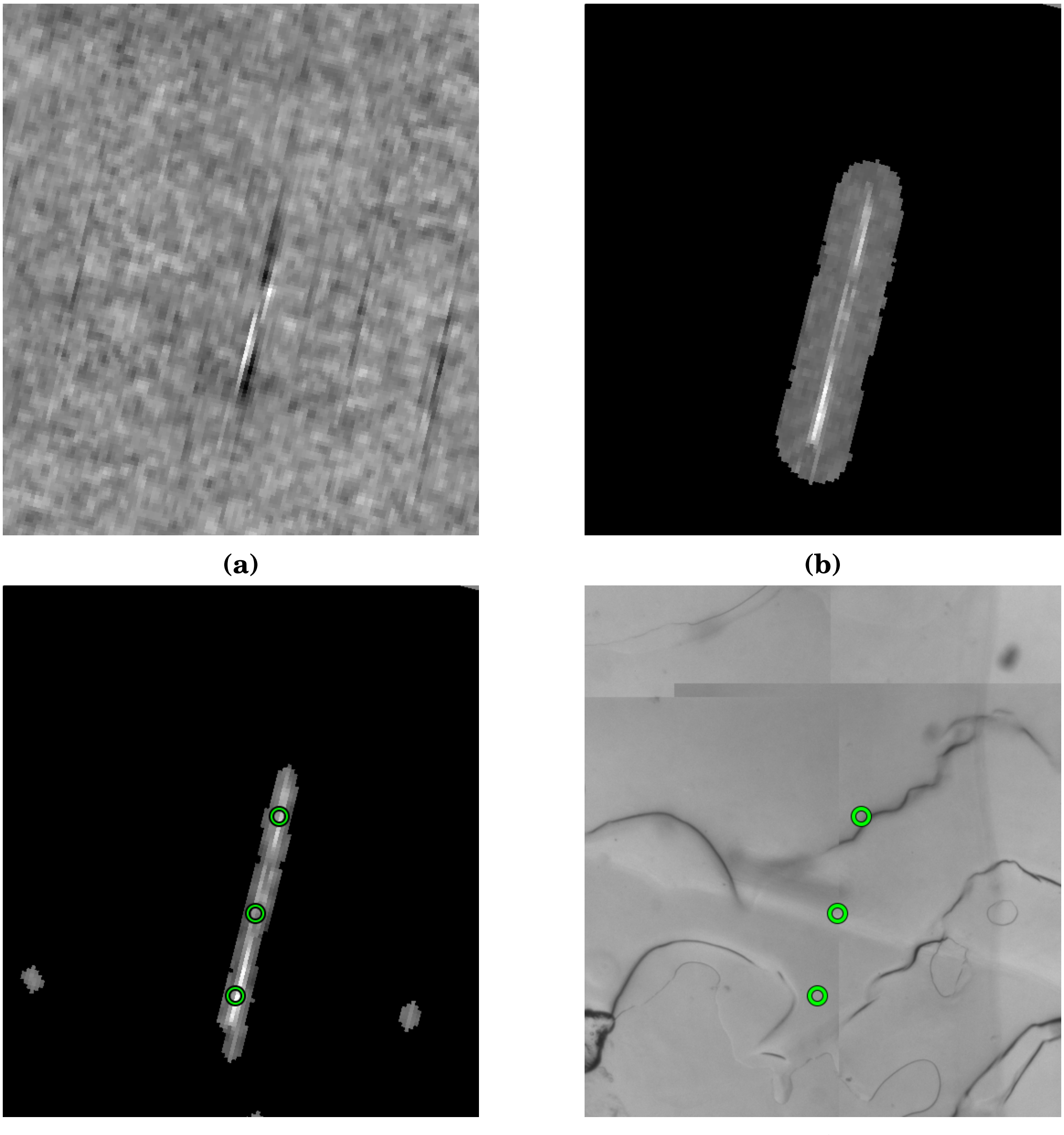
(a)
(b)
(c)
(d)

Figure 4.10: A comparison showing how each quantification method dealt with an incorrectly mitigated streak artifact. (a) A streak artifact in one slice of the CT image. Note that the very bright voxels were accompanied by very dark voxels. (b) A MIP of the region that was correctly determined to have no microspheres by the NBG method. (c) A MIP of the region that was incorrectly determined to have 3 microspheres by the WBG method. (d) The corresponding area of the optical image where WBG estimated 3 microspheres were present.

and a majority of that error arose due to errors in stage II. Given that those values do not include the error due to incorrect localization in the direction normal to the microsphere plane, it is likely that the true MAE is slightly larger. Reducing the dimensionality of the dose map reduced the dose distribution error by less than two percentage points, which suggests that the error due to incorrect localization in a single dimension had a fairly minor effect on the overall accuracy.

Fairly evaluating the method requires dealing with limitations inherent to the phantom. As noted in figure 4.4, the microspheres in the phantom periphery shifted, which was mitigated by excluding the periphery. While peripheral motion due to agar desiccation and contraction was fairly obvious, there may also have been microsphere motion within detected regions that could only have been observed by optically scanning the phantom before and after the CT scan. A better way to prevent motion would be to use a background medium that cures, is optically transparent, and has a similar attenuation coefficient to tissue, such as the epoxy used by Marxen *et al.* [47]. If concerns about microsphere motion were fully addressed, then acquisition parameters could be changed to improve detection. For example, when the phantom was scanned with twice the exposure time to reduce noise in detected phantom regions, the number of spurious regions was reduced, but overall accuracy suffered due to more microsphere motion during the longer scan. If a scan that just reduced noise without increased motion were used, it could potentially improve microsphere quantification results, which account for most of the dose distribution error observed in the method.

Another potential source of errors in the phantom is bubbles in the agar. Some large bubbles are visible in figure 4.4c, but bubbles around the same size as the microspheres are harder to distinguish from spheres in the optical microscope image. Examples of this are shown in figure 4.11. It is possible that different background materials would not have the same issue with bubbles as agar. If that is not the case, then a high-resolution x-ray image of the phantom could be used to identify hard-to-discern bubbles and improve the evaluation of algorithm performance.

4.4.1 Transition to tissue specimen

The single example tissue specimen detailed in figure 4.9 elucidates the new information that may be realized with this method. Archived tissue specimens from tumor and normal liver tissue in patients that have received ^{90}Y RE and subsequent liver transplant are plentiful at transplant centers [78], and the described method for non-destructively mapping the 3D microscopic distribution of microspheres using micro-CT may be key for future understanding of the radiobiologic effects of RE. However, additional work outside the scope of this manuscript may still be required for accurate microdosimetric evaluation

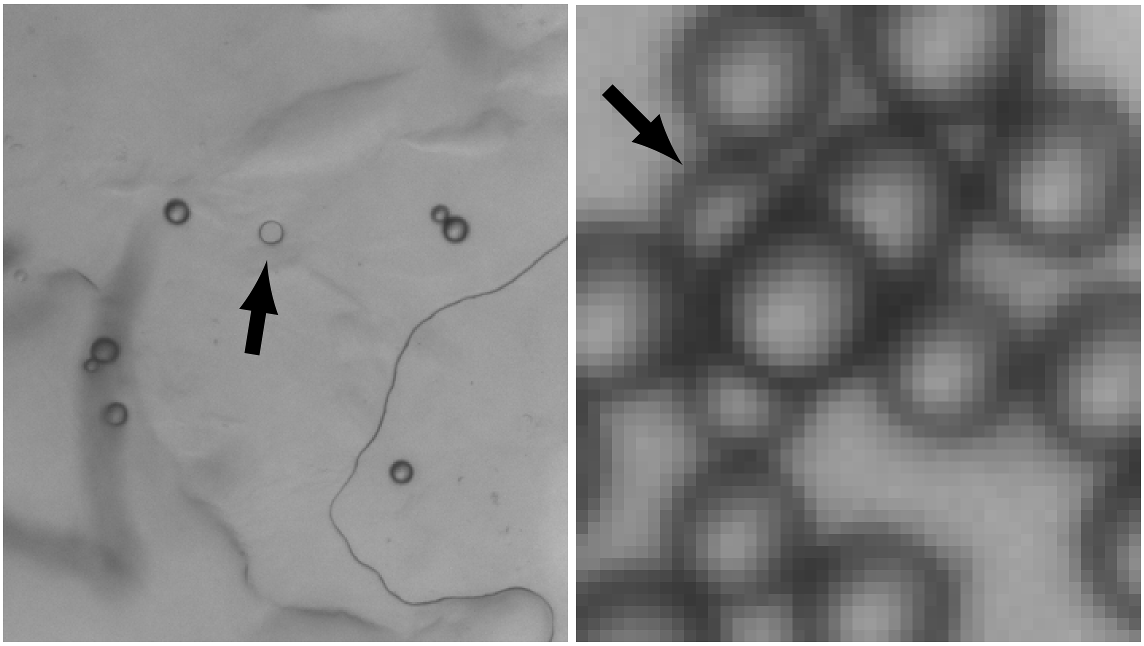

(a) **(b)**

Figure 4.11: (a) An example of a difficult-to-distinguish bubble in the agar phantom. The central circular shape differed in appearance from the 7 microspheres surrounding it. (b) An example of questionable microspheres. These were marked as true microspheres, but the strange shapes of one or more spheres surrounding the largest, central microsphere suggest that some of the displayed spheres may have actually been microsphere-sized air bubbles.

in tissue samples including: accounting for lack of charged particle equilibrium at tissue boundaries, sphere movement between treatment and explantation of liver tissue, and tissue volume changes during tissue fixation and preservation.

4.5 Conclusions

This work presented a method for studying 3D glass microsphere distribution in large, unsectioned tissue blocks. The method is based on the combination of high-resolution micro-CT scans of the sample and a multi-stage algorithm that detects regions containing microspheres, estimates the number of microspheres in each region, and estimates the location of each sphere within the scanned block. This algorithm was validated by scanning a phantom with known microsphere locations and comparing the dose map generated using the estimated locations to the true dose map. The algorithm's utility was demonstrated by detecting microsphere locations and estimating the dose map for a human tissue sample of a neuroendocrine tumor that was treated with glass microspheres prior to excision.

This method can be used to detect microsphere quantities and locations with accuracies that far exceed what is possible using state-of-the-art PET scans [79] using a less time- and labor-intensive process than sectioning, staining, and optical scanning. The ability to more simply and accurately calculate dose and detect microsphere clustering in larger tissue sections could yield important insights on how glass microspheres cluster in normal and tumorous tissue and improve radioembolization treatment planning.

Chapter 5

Comparison of Actual and Simulated Microsphere Distributions

5.1 Introduction

The ability of the HAT generation method and the particle transport and trapping method described in chapter 3 to predict the risk of toxicity in normal liver tissue depends on the accuracy of the simulated distribution of microsphere cluster sizes. Walrand *et al.* simulated a microsphere distribution and showed that, when used with their proposed radiobiologic model, it produced reasonable predictions for the survival of normal liver tissue. A critical aspect of their results was that a sufficiently heterogeneous dose distribution would spare lobule structures frequently enough that surviving lobules could compensate for the damaged or dead lobules. The heterogeneity of the dose distribution is directly impacted by the clustering behavior of the microspheres. However, like the work presented in chapter 3, clusters of that simulated distribution were not verified to be physically realistic [10, 11].

Högberg *et al.* carefully measured the clustering behavior of resin microspheres in several samples of normal human liver tissue and used that information to propose a novel trapping model that produced clusters consistent with their observations [51, 70]. This method modeled the HAT as a balanced binary tree, which differed substantially from the branching structures observed in true liver vasculature. Also, there are several notable differences between resin and glass microspheres, including differences in size distribution, density, specific activity, and in the total number of microspheres used in treatment [19]. Furthermore, resin microspheres, unlike glass microspheres, aggregate when suspended in a saline solution [19]. A typical resin microsphere treatment contains between 20 and 60 million spheres, while glass microsphere treatments usually administer less than 2 million spheres [30]. Kennedy *et al.* compared glass and resin microsphere distributions qualitatively and did not observe notable differences [69], but given the different administered quantities there must either be a difference in the total number of clusters or in the number of microspheres contained in those clusters [51]. This suggests that clustering information from resin-microsphere treatments cannot be directly used to predict glass microsphere clustering behavior.

To understand the risk of toxicity for treatments of glass microspheres, a characterization of glass microsphere clustering is necessary. Chapter 4 discussed a novel method to characterize glass microsphere distributions in whole tissue samples using micro-CT. Applying that method to large, treated porcine liver samples should allow characterization of a large number of microspheres in treated tissue, and comparison with simulated microsphere clustering.

5.2 Materials and methods

The use of animals in this work was performed under IACUC approval.

To verify the clustering behavior in the microsphere distributions simulated using the HAT model from chapter 3, it is necessary to examine microsphere distributions in normal liver tissue. Due to the similarity of the vascular structure of porcine and human livers [80] and a dearth of preserved normal human liver tissue samples, a characterization of the microsphere distribution in a normal porcine liver was attempted for this work.

5.2.1 Treated porcine liver sample

An approximately 321 MBq TheraSphere treatment was administered to a juvenile pig 292 hours after calibration time, which corresponded to a whole-liver dose of 53 Gy. After administration, the pig was maintained alive for several weeks to observe complications due to treatment before the pig was sacrificed and the liver was explanted and stored in Formalin prior to imaging.

The liver was divided into two equally sized pieces and imaged using a Bruker SkyScan 1176 micro-CT scanner (Bruker MicroCT, Kontich, Belgium). The scanner allowed large samples to be imaged at high resolution by moving the scanner bed. The approximate dimensions of each imaged liver piece was 5x5x11 cm. A total of 708 projections were acquired for each bed position at a tube voltage of 80 kVp and an exposure of 1.8 mA s. Other relevant scan parameters were unchanged and are described in chapter 4.

After imaging the liver samples, microsphere locations in one sample were estimated using an algorithm based on the NBG method described in chapter 4. Because the sample was much larger than the phantoms scanned in chapter 4, the background variance was expected to be significantly higher and required a different set of region detection parameters to reduce the expected number of FPs.

To review the relevant portion of chapter 4 briefly, the process of estimating parameters and measuring detection method performance was done using thin phantoms composed of glass microspheres embedded in agar and sandwiched between two coverslips. These were scanned using a high-resolution optical microscopy to determine the true microsphere locations, and then scanned in the same micro-CT system used for the liver slices. The region-detection stage of the microsphere detection algorithm was applied to the first phantom to estimate $\hat{\zeta}$, the scalar used in the NBG method to relate the sum of the voxels identified during region detection to the number of microspheres found in those regions. The same detection parameters and the estimated scalar were then applied to a second phantom in order to find regions, estimate microsphere quantities in those regions, and measure the performance of the microsphere detection algorithm.

Experience with the phantoms showed that microspheres were generally easy to identify visually. Using the parameters that worked best for the thin phantoms and tissue specimens on the large liver samples identified areas that did not appear to contain microspheres. Higher thresholds and larger minimum regions were tested with the phantoms, and values that produced the best visual results in the livers while maintaining acceptable TPFs and FPFs using the phantoms were used for the analysis. After microsphere quantities were estimated in regions of the porcine liver, microsphere locations were estimated using the weighted k-means algorithm described in chapter 4.

After microsphere locations were estimated, the locations were partitioned into clusters by grouping detected microspheres that were closer than 200 µm.

5.2.2 Microsphere transport model

With the microsphere distribution characterized as described above, it was then possible to verify the clustering behavior of simulated microsphere distributions created using a variety of microsphere infusion models. These methods were based on the simulated particle transport model described by Walrand *et al.* [10]. All methods modeled particle infusion as a process where a single microsphere was placed in an initial vessel and was carried through the tree until the microsphere arrived at a trapping vessel. When the microsphere encountered a bifurcation, it randomly entered one child vessel or the other probabilistically. The probability of a microsphere entering either vessel depended not only on the relative flow of blood in the two branches, but on the vessel geometry. This combined dependence on both flow and geometry was based on work by Kennedy *et al.* that used fluid dynamics simulations of microspheres traversing a two-generation vessel tree. Each of the four output vessels had equal blood flow, but the flow of microspheres through the children vessels was nevertheless unequal due to differences in vessel geometry. Walrand *et al.* assumed that microspheres were slightly more likely to enter the child vessel most aligned with the parent vessel (referred to as the straighter vessel) and less likely to enter the less-aligned vessel (referred to as the more bifurcating vessel). They then showed that images produced with that assumption were more heterogeneous and more qualitatively similar to microsphere distributions observed *in vivo* with PET imaging. The probability of a microsphere entering either vessel at a bifurcation was given by Walrand *et al.* as

$$P_b = \frac{D_b p}{D_b p + (1 - D_b)(1 - p)} \tag{5.1}$$

$$P_s = 1 - P_b, \tag{5.2}$$

where P_b and P_s are the probabilities of the microsphere entering the more bifurcating and the straighter vessel, respectively, D_b is the ratio of blood flow through the more bifurcating vessel and the parent flow, and p is the probability of a sphere entering the more bifurcating vessel for equal child outflow. Based on Kennedy's work, Walrand chose $p = 0.4$.

Using this general framework, the infusion methods investigated in this work can be classified by their handling of two orthogonal concepts: embolic (EM) versus non-embolic (NE) methods and diameter-aware (DA) versus diameter-unaware (DU) methods. Embolic methods assume that the trapping of microspheres in vessels inhibits the flow of blood in that vessel and parent vessels, while non-embolic methods assume that blood flow is unchanged regardless of how many microspheres trap in a vessel. The change in flow to each vessel requires P_b and P_s to be updated for all vessels in the tree after a microsphere traps, and generally reduces the maximum number of microspheres found in trapping vessels due to the reduced likelihood of microspheres reaching each one. Non-embolic infusion methods do not adjust the flow as microspheres trap, which increases the maximum number of microspheres that cluster in trapping vessels.

Another aspect of infusion models is if the diameters of microspheres and the vessels through which they flow are considered when determining trapping locations. Diameter-unaware methods assume that all microspheres trap in THAs, regardless of the diameters of the microspheres and vessels involved, while diameter-aware infusion models trap microspheres in higher-order vessels if child vessels are too narrow to admit the microsphere. When a microsphere arrives at a bifurcation in a diameter-aware method, it is trapped if the microsphere diameter exceeds both children vessel diameters (or if a larger microsphere is already trapped there), it enters the larger vessel if only one vessel diameter is smaller than the microsphere, and it enters either vessel randomly, as described by (5.1) and (5.2), if both vessels are large enough to admit the microsphere. Restricting microsphere flow based on vessel and microsphere diameters effectively reduces the number of potential trapping locations.

A model of the HAT was generated as described in chapter 3, and ten microsphere distributions were simulated within that tree for each combination of infusion methods described above, specifically diameter-unaware, non-embolizing (DU-NE), diameter-unaware, embolizing (DU-EM), diameter-aware, non-embolizing (DA-NE), and diameter-aware, embolizing (DA-EM) infusion simulations. The same cluster analysis was performed on the simulated microsphere locations as the micro-CT image, where microspheres within 200 µm of other microspheres were grouped into the same cluster. The number of microspheres used for each simulated infusion was proportional to the number-density of microspheres in the porcine liver, but scaled to the XCAT liver volume.

The distribution of cluster sizes was then compared between the 4 simulated methods and the detected clusters from the porcine livers to determine which simulation method produced the most realistic clusters. Due to the large number of microspheres in the simulation, attempts to directly perform single-linkage clustering failed due to lack of memory. However, as portal tracts are spaced at least 600 µm apart, it is possible to approximate cluster sizes by iteratively grouping vessels with microspheres through shared parent vessels, provided the distance between spheres in child and parent vessels doesn't exceed 200 µm. Images with resolution similar to that of ^{90}Y PET were also simulated, as explained in chapter 3, by generating a volume image with 2 mm pixel widths and convolving it with a 3-dimensional Gaussian filter with FWHM 8 mm. A single coronal slice from near the center of the volume was extracted from a representative microsphere distribution for each microsphere transport model described above.

5.3 Results

5.3.1 Treated porcine liver sample

A representative liver sample that has been prepared for micro-CT imaging is shown in figure 5.1.

A slice of the micro-CT image of the liver sample is shown in figure 5.2. Several clusters of microspheres are clearly visible.

The parameters for region detection and sphere quantification were chosen, and their performance was verified, using the phantoms from chapter 4. Regions with more than 25 connected voxels that were at least 2,000 HU above background were identified as regions of interest, and $\hat{\zeta}$ from the NBG method was estimated to be $1.68 \cdot 10^{-6}$ spheres per HU using one of the phantoms and a dilation radius of 3. Performance was estimated using these values in a different phantom. In that phantom, regions were detected that contained 83% of microspheres, and quantification in those regions resulted in a TPF of 0.74 and a FPF of 0.036.

The liver sample was then processed with those same parameters, and it was estimated that 838,102 microspheres were present in 128,877 separate

Figure 5.1: An example of a treated and resected porcine liver that has been divided to allow it to be imaged with a high-resolution micro-CT scanner.

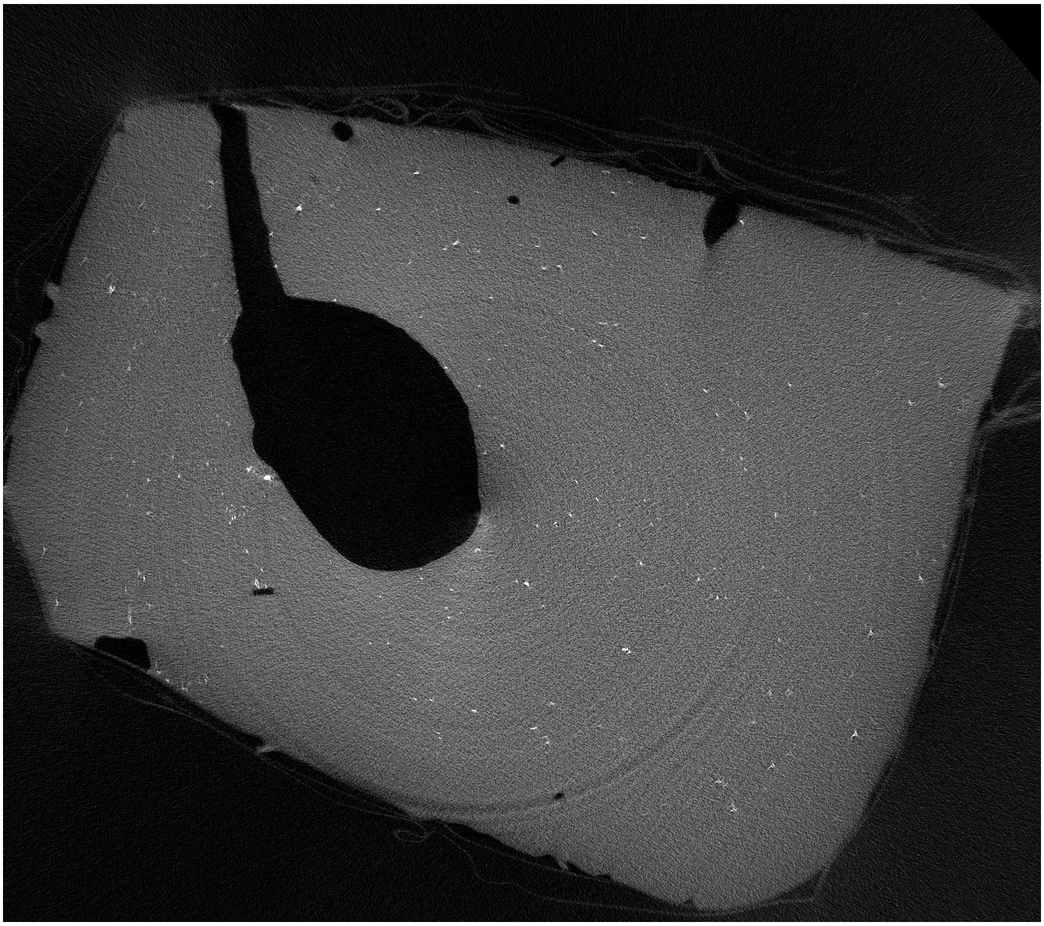

Figure 5.2: A slice from a micro-CT image of a 144 mL porcine liver sample that received an approximately 53 Gy glass microsphere treatment. Bright spots in the object are generally clusters of one or more microspheres.

clusters. A representative area of the tissue sample is displayed in figure 5.3. Based on a segmentation of the micro-CT image, this gave a microsphere number-density of approximately 5,820 microspheres per mL of liver. A histogram of the cluster distribution with a bin width of 10 spheres is shown in figure 5.4.

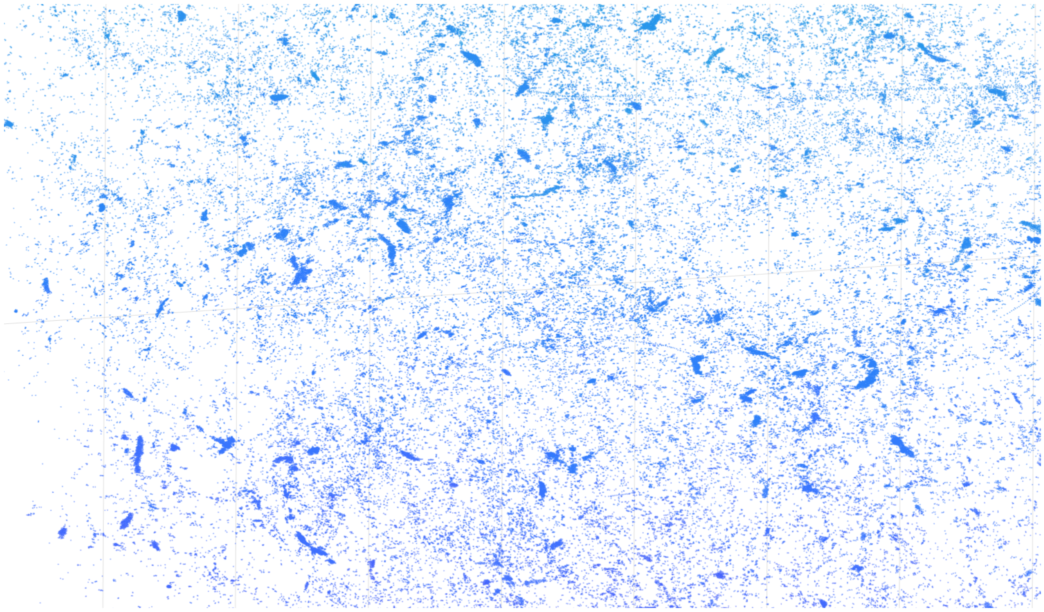

Figure 5.3: A representative section of the locations estimated by the microsphere detection algorithm when applied to the porcine liver image. Note the highly heterogeneous pattern; while many microspheres appear isolated, many are aggregated into clusters.

5.3.2 Microsphere transport model

The simulated HAT contained 1,849,267 portal tracts, which translated to roughly 4.8 million THAs with an average diameter of about $13\,\mu\mathrm{m}$ for a physically realistic blood flow of $400\,\mathrm{mL/min}$. The tree also contained approximately

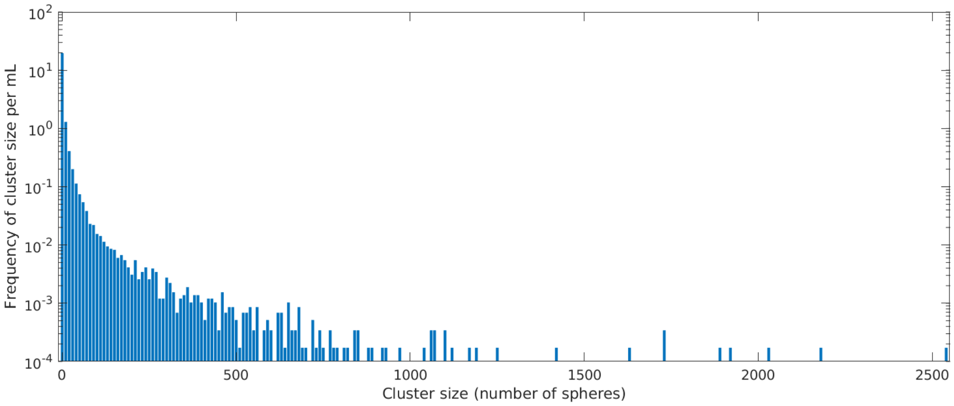

Figure 5.4: A log-scaled histogram of the incidence of clusters of different sizes per mL in a 144 mL porcine liver sample, aggregated into bins of 10 elements.

550,000 vessels greater than the average TheraSphere diameter that either had no child vessels, or had only children vessels smaller than the average sphere diameter (i.e., potential trapping vessels). That tree is shown in figure 5.5.

A cluster-size histogram, created from the 10 simulated infusions for each model, is displayed in figure 5.6. All microsphere-infusion models produce cluster distributions that predominantly have single-spheres, but diameter-aware methods more frequently contain larger clusters, resulting in a histogram with a longer tail. This is reflected in the maximum cluster size for each method. For the DU-NE method it is 111 spheres, for DU-EM it is 50 spheres, for DA-NE it is 339 spheres, and for DA-EM it is 64 spheres.

The same slice of a simulated activity image at PET resolution was generated using each infusion model and is shown in figure 5.7.

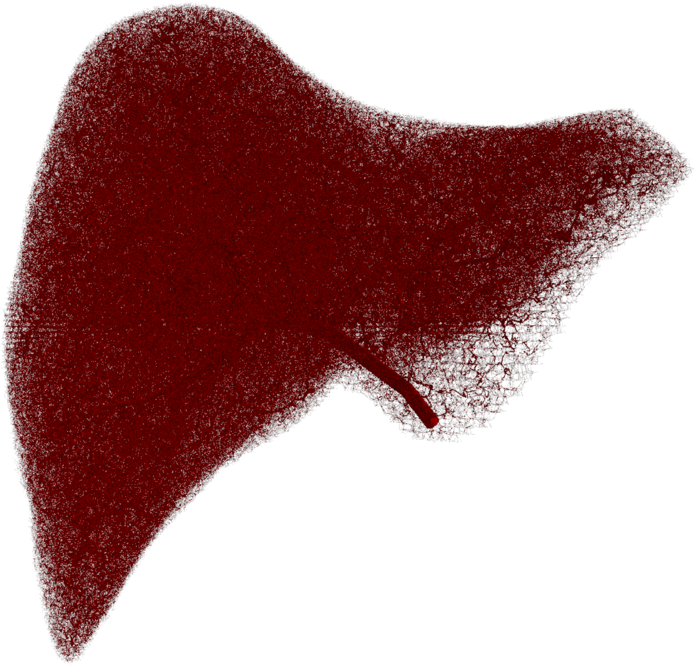

Figure 5.5: The hepatic arterial tree used for microsphere infusion simulations. It contains approximately 1.8 million portal tracts and the average terminal hepatic arteriole is 13 µm.

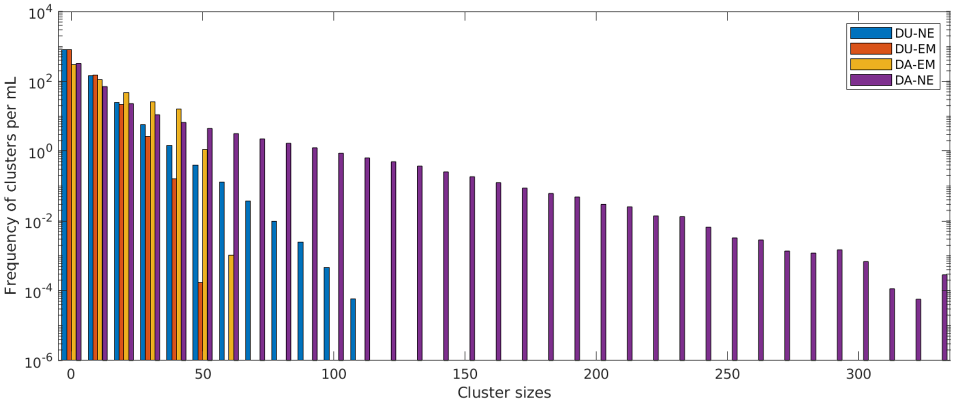

Figure 5.6: A log-scaled histogram comparing the frequency per mL of clusters using the diameter-unaware non-embolizing (DU-NE), diameter-unaware embolizing (DU-EM), diameter-aware non-embolizing (DA-NE), and diameter-aware embolizing (DA-EM) methods.

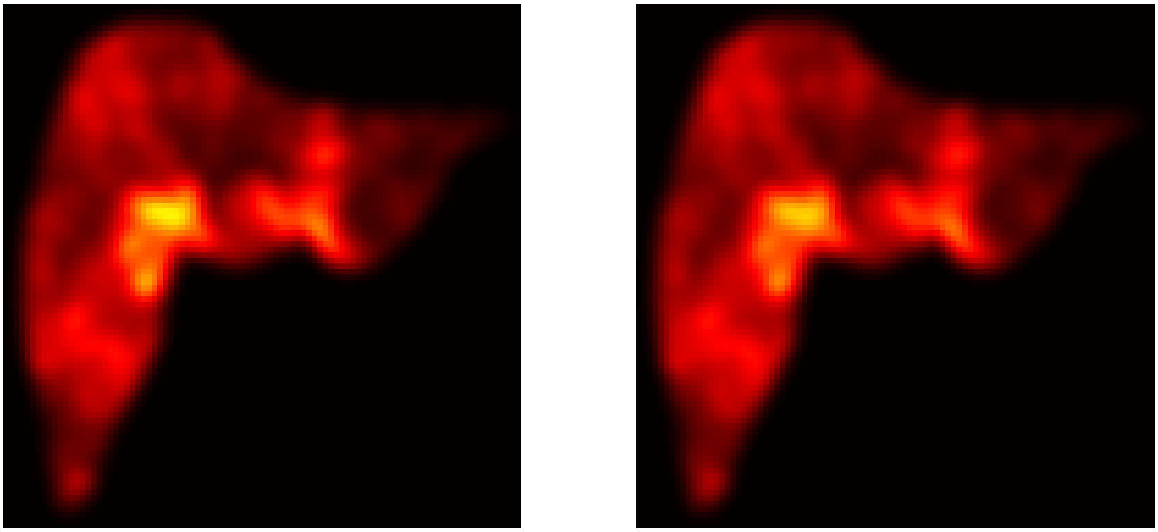

(a) DU-NE **(b)** DU-EM

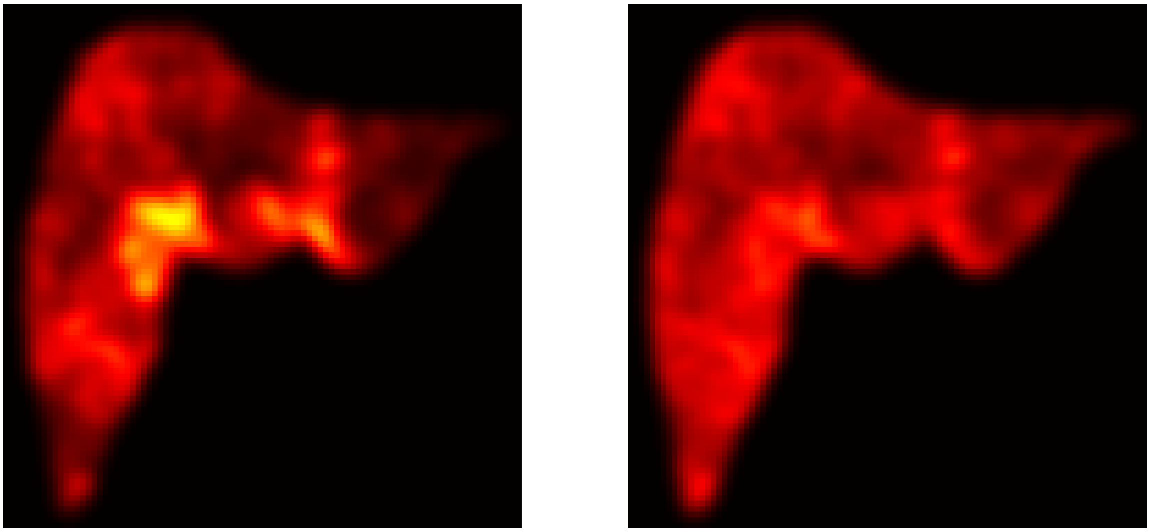

(c) DA-NE **(d)** DA-EM

Figure 5.7: Representative slices of simulated dose images generated using the four microsphere infusion methods described in this work. Non-embolic methods are always more heterogeneous than embolic methods, but diameter awareness has a more complicated effect on distribution heterogeneity. If the method is non-embolic, diameter awareness increases heterogeneity, but for embolic methods it has the opposite effect.

5.4 Discussion

This work shows that microspheres within normal porcine liver tissue aggregate into much larger clusters than predicted by previous models of microsphere infusion and trapping [10, 68]. Thus, trapping models that result in larger clusters like those observed in the liver sample likely produce more realistic micro-scale dose distributions that could be a useful predictor of normal liver tissue toxicity for different treatment plans.

The greater noise present in large tissue samples resulted in larger FPFs than were observed in the thin phantoms used to verify this method. That necessitated a much higher detection threshold, which likely increased the FN count. While the FN increase can be estimated using phantom data, the increase in FPs is more difficult to predict. Thus, while chapter 4 demonstrated that glass microspheres can be detected with high accuracy and few false positives in both thin phantoms and reasonably thin tissue samples (around 1 cm), more work is necessary to fully understand algorithm performance in the presence of noise observed in larger tissue samples.

However, it was observed using the phantom that nearly all FNs were isolated microspheres, and at lower thresholds, spurious regions caused by noise were almost all estimated to have fewer than two microspheres. In larger clusters, misestimations of only one or two microspheres per cluster were observed.

This suggests that, in spite of noise, the very large clusters observed in this work are representative of actual microsphere clustering behavior, and thus accurate particle transport and trapping simulations must produce similarly large clusters. Further evidence supporting this fact is that the total activity of the microspheres infused into the pig is consistent with the number-density of microspheres detected in this work.

Of the different distribution methods tested above, the DA-NE method produced the most realistic distributions of microspheres at the number-density observed in the porcine liver sample. Figure 5.6 shows that the embolizing methods seldom had clusters larger than 50 spheres (the maximum allowed in a THA), while the DA-NE infusion method produced larger clusters. Walrand observed that modeling embolic effects tended to create a less heterogeneous distribution of microspheres [10]. This was also observed using the infusion models in this work.

However, diameter awareness when determining trapping locations had a more complicated effect on cluster sizes and the heterogeneity of the images shown in figure 5.7. If embolic effects were being modeled, then the microspheres were more evenly spread among a smaller set of trapping locations, which reduced heterogeneity, as shown in 5.7d. However, figure 5.7c shows that diameter awareness without modeling embolic effects on blood flow increased the heterogeneity, as microspheres that might have formed clusters downstream of a narrow vessel instead formed one large cluster in a higher-order vessel.

The improved accuracy of non-embolizing methods was unexpected, as the embolizing method discussed by Walrand *et al.* seemed like a more realistic model of particle infusion and trapping due to its simulation of decreasing blood flow as microspheres trap. However, these results suggest that non-embolizing methods may be a more accurate model of the infusion process, and given that glass microspheres are injected in a single bolus [48], microsphere traversal of the vessel tree is likely not substantially impacted by flow changes between the trapping of different microspheres.

There are still important differences between the true and simulated cluster distributions. For example, the relative incidence of small cluster sizes is much higher with all simulated distributions, and even the DA-NE model produces far fewer large clusters than observed in reality. This suggests that models of microsphere trapping that result in even larger clusters may produce more realistic distributions.

5.5 Conclusions

The accuracy of microsphere distributions simulated in this work is important for predicting the likelihood of toxicity in normal liver tissue treated with glass microspheres. Using micro-CT imaging of a large treated liver sample, this showed that microsphere clusters found in normal porcine liver tissue had larger cluster sizes than predicted by previous simulation methods. A new model of particle transport and trapping was proposed and shown to produce more realistic clusters. More accurate simulation of microsphere distributions would provide more accurate estimates of the dose distribution in the liver. This would allow comparing different treatment plans, such as varying numbers of microspheres with different activities per microsphere, through simulation, which could lead to improved treatment planning and patient outcomes.

Chapter 6

Summary and Future Work

6.1 Summary

The incidence of liver cancers is increasing worldwide, and better treatment options are necessary to improve patient outcomes. Radioembolization (RE) is a palliative treatment option that is increasingly used in conjunction with curative treatments to increase their applicability and effectiveness. Improved treatment planning has the potential to improve the efficacy of this therapy, potentially providing curative treatment or increasing the number of patients qualifying for curative therapies. RE targets liver tumors by inserting millions of microspheres into the hepatic artery and allowing them to be carried by the flow until they trap permanently in the vessels and deposit radiation in surrounding tissues. Those tissues are likely to be tumorous, as tumors in the liver promote artery growth to access highly oxygenated arterial blood. While very high absorbed doses to the liver are possible in RE, precisely how normal liver tissue survives is not well understood. But, there is ample evidence that tissue survival depends in part on the heterogeneity of the dose, which in turn depends on the distribution of microspheres within the liver. Non-uniform microsphere trapping produces a highly heterogeneous dose that may allow enough normal tissue to survive that sufficient liver function is retained for the patient to survive the therapy. However, without accurate predictions of how treatment plans affect toxicity, plans may not deliver a high enough absorbed dose to tumors to achieve control.

There are a number of variables that can be used to plan therapy, including the number and activity of the spheres. The ability to model both a patient's hepatic arterial vasculature and the flow and trapping of microspheres within it could enable improved predictions of the probability of liver toxicity and tumor control for different possible treatment plans. Previous work modeling the hepatic arterial tree has produced models that have physically unrealistic aspects, and simulated microsphere distributions have not been verified to approximate true microsphere distributions, limiting their utility in understanding the radiobiological characteristics of RE therapy and thus treatment planning.

Furthermore, three-dimensional cluster analysis of glass microspheres has not been performed on large sections of normal liver tissue, as traditional methods for characterizing microsphere locations is time-consuming, manual, and most commonly performed in two dimensions. Without a representative analysis of glass microspheres in normal liver tissue, attempts to estimate absorbed doses using computational models cannot be relied upon to provide realistic dose distributions.

This work has proposed a physically realistic model of the hepatic arterial tree and models of microsphere transport and trapping that allow the simulation and comparison of RE treatment plans. It has further demonstrated a novel method to detect, quantify, and estimate the locations of microspheres within large tissue sections without costly manual processing through the use of high-resolution micro-CT imaging and automated sphere quantification and localization algorithms. Finally, it has shown, using cluster analysis, that different models of microsphere transport varied in their ability to simulate physically realistic microsphere distributions. This provides data and direction needed to further refine models of liver vascular anatomy and microsphere trapping to allow them to be relied upon as tools for improved treatment planning of RE.

6.1.1 Hepatic arterial tree model

In order to simulate realistic distributions of microspheres suitable for micro-scale dose analysis, a major achievement of this work was to generate a physically realistic, highly detailed model of the hepatic arterial tree. While previous work had created both a coarse, physically realistic model and a highly detailed, but physically unrealistic model, this work demonstrated how to achieve both aims.

First, it showed how to create a realistic tree by following three physically based laws: conservation of matter, which ensured that the amount of blood flowing into a vessel was the same as the amount flowing out of it; Murray's law, which related the diameters of a parent vessel with those of its children vessels using a bifurcation constant; and Poiseuille's law, which related the drop in pressure from the input to the output of a vessel to the vessel's length, diameter, and blood flow. This work proposed a method to estimate Murray's bifurcation constant using measurable features, such as vessel diameters and blood pressure. Additionally, the angle at which vessels connected must also be guided by physically realistic optimization principles. This work chose vessel connection points that minimized the drag of blood flow on vessel walls, as it required only local information and research has shown that this factor is an important influence on vessel branching structure observed in nature.

The actual tree was generated using a macrocell growth method based on segmentations of the liver and the hepatic artery taken from the XCAT phantom. The method could be readily applied to liver anatomies and vascular trees derived from patient data to produce a patient-specific liver model. Macrocell growth methods generate realistic vasculature by simulating the growth of the organ and its vasculature from a small shape to its full size over a series of cycles. During each cycle, the shape is filled with macrocells that must be connected to existing vessels. Once the shape is filled and all macrocells are perfused, the shape is grown, (causing the macrocells to spread apart). New macrocells are then created to fill the now empty spaces between existing macrocells.

The hepatic arterial tree models generated using this method were validated by comparing the derived physical parameters to those reported in literature. In particular, the terminal hepatic arterioles matched literature values well, which was important when performing microsphere transport and trapping simulations.

6.1.2 Microsphere detection via micro-CT imaging

While producing physically realistic models of the hepatic arterial tree should improve the simulation of RE and associated toxicities, if the clustering behavior of a true distribution is unknown, then the accuracy of simulated microsphere distributions is likewise unknown and cannot be relied upon to provide useful information for understanding hepatic toxicity or treatment planning. Traditional methods of assessing microsphere locations and clustering in tissue samples require the samples to be sectioned, stained, scanned, and manually scrutinized in a time-intensive process. Additional care is necessary if three-dimensional location or clustering information is required. Due to this, only small tissue samples have typically been examined.

In order to detect and estimate microsphere locations in large tissue sections more easily, this work developed a novel method using micro-CT imaging and automated image analysis procedures. This was possible due to the high attenuation coefficient of glass microspheres compared to normal liver tissue. The quantification and localization process was implemented in three stages. First, regions potentially containing microspheres were identified by simply choosing contiguous voxels having values higher than a particular threshold value. The sum of those voxels relative to the attenuation coefficient of the surrounding medium was calculated and used to estimate the number of microspheres present in each detected region. To mitigate the effect of image degrading factors on quantification, adjoining voxels were also used in the calculation. Finally, the detected regions and the estimated number of spheres in each region were used by the localization algorithm to estimate three-dimensional locations for each microsphere.

CHAPTER 6. SUMMARY AND FUTURE WORK

This analysis method was verified by creating very thin phantoms composed of agar and microspheres that could be scanned by a micro-CT system as well as by transmission-light microscopy to determine gold-standard microsphere locations. The scalar relating the integrated intensity above background in a region to the number of microspheres in that region depended on the threshold, the minimum number of voxels in a region, and on the number of adjoining voxels used to quantify the microspheres. Thus, the scalar was estimated using those region detection parameters on one phantom, then the same parameters and the newly estimated scalar were used on a different phantom to estimate performance data. Total performance of the method was measured by calculating the mean absolute error between the dose map created with the true microsphere locations and the map created with the estimated locations.

The microsphere detection algorithm was then applied to a paraffin-embedded human tissue sample that had been resected after radioembolization with glass microspheres. The algorithm performed well, correctly detecting $> 93\%$ of embedded microspheres with $< 5\%$ of detections being false positives.

After verification, a pig was treated with glass microspheres prior to being sacrificed and having its liver scanned via micro-CT. The microsphere distribution in the liver was estimated for one sample that was approximately 5x5x11 cm, and cluster analysis was performed to characterize the estimated locations.

6.1.3 Microsphere transport and trapping models

The resulting microsphere clustering data from the normal liver tissue samples allowed different microsphere transport and trapping models to be evaluated.

Previous models simulated microsphere trapping by sending microspheres from the initial vessel to the randomly selected trapping vessels consecutively. When the microsphere arrived at a bifurcation, either the straighter or more bifurcating vessel was chosen based on a combination of the relative blood flow and the relative geometry of the child vessels. Previous models assumed that all microspheres trapped in terminal hepatic arterioles, without consideration of the diameters of the microspheres or intervening vessels. These models differed in whether a trapped microsphere reduced flow to that vessel or not. If a trapping model was embolizing, then the blood flowing to an embolized vessel was reduced by some fraction that increased as more particles trapped in it. This in turn reduced the likelihood of microspheres arriving in that vessel, with the overall effect that the microsphere distribution was more homogeneous. In contrast, non-embolizing methods assumed that blood flow remained constant, regardless of the number of microspheres present in a vessel. This tended to create large clusters and an overall less homogeneous microsphere distribution.

Another aspect of microsphere transport, proposed in this work, is whether microspheres always arrive in terminal arterioles, or if they can be trapped in higher-order vessels within the tree. Most terminal hepatic arterioles are less than half the diameter of an average microsphere, and thus microspheres are likely to be trapped in non-terminal arterioles too. Diameter-aware models consider both the diameter of a microsphere and diameters of the vessels it passes through as it travels through the vasculature.

Because these concepts are orthogonal, they were combined to create four different microsphere transport and trapping models: diameter-unaware and non-embolizing, diameter-unaware and embolizing, diameter-aware and non-embolizing, and diameter-aware and embolizing.

In order to compare the microsphere clusters formed using each trapping model, ten microsphere infusion simulations, consisting of approximately 10 million microspheres each, were performed for each trapping model, and cluster analysis was performed on the resulting microsphere distributions. The number of microspheres simulated was chosen to produce the same microsphere number-density as observed in the porcine sample.

A histogram of the observed microsphere cluster sizes in the porcine sample showed that while small microsphere cluster sizes were most common, there were also many large clusters of detected microspheres, several with more than 1,000 spheres. Histograms of the cluster sizes of each transport and trapping method were also generated, and the method that considered both the diameters of the spheres and the vessels without modeling embolic effects produced cluster-size distributions most similar to the porcine liver sample. These findings have important implications for understanding liver toxicity in RE and for refining microsphere trapping models.

6.2 Future work

This work has yielded interesting insights into the distribution of microspheres in treated tissue and the accuracy of infusion simulations intending to replicate those distributions. There are also several potential research directions that could improve the accuracy of the simulations and increase potential applications for this work.

6.2.1 Hepatic arterial tree model

Currently, the simulated arterial tree is generated using segmentations taken from the XCAT phantom. Simulations using segmentations taken from patient data could demonstrate the utility of these models for treatment planning; however, that would likely require the ability to model the presence of tumors within normal tissue. The morphology of tumor vasculature is generally more complicated than normal liver vasculature, and blood flow within those vessels is erratic, sometimes resulting in blood flowing in different directions at different times within the same vessel [22]. However, it may be possible to approximate microsphere distributions in tumors sufficiently well to make realistic predictions of both tumor dose and normal tissue toxicity.

In a similar vein, additional data taken to support other aspects of treatment planning, such as contrast-enhanced CT or MR angiography and perfusion measurements, could be used to increase the accuracy of microsphere distributions. While current work aims to allow the prediction of overall survival and does not predict the specific dose distribution, it is possible that future simulations could do so by incorporating more existing sources of data.

6.2.2 Micro-CT detection of glass microspheres

While the performance of glass microsphere detection and localization appeared very good when verified using thin phantoms, larger tissue samples have higher noise, which can result in a higher, but currently unknown, number of false positives. During the phantom preparation process, embedding the phantoms in larger water phantoms was discussed and rejected due to concerns that the water could cause microspheres to shift in the agar. If the phantoms were instead formed by embedding glass microspheres in tissue-equivalent resin that was allowed to cure prior to imaging, the phantom could be submerged in differently sized, water-filled cylinders to approximate tissue samples and verify performance at different noise levels. Such phantoms would also avoid issues with microsphere shifting that was a confounding factor of the longest scans in chapter 4.

Resin-based phantoms would also be more durable, which means they could also be shipped to different institutions and used to measure performance of other micro-CT scanners, allowing multi-institutional collaboration.

Higher noise levels may also require different methods to accurately detect microspheres. With the porcine liver samples, it was necessary to use a higher detection threshold to avoid excessive false positives, but this likely resulted in more false negatives. If the sphere quantification stage were better able to reject false positives, then the detection threshold could be lowered, resulting in fewer false negatives. One aspect of the regions that is mostly ignored is the texture. It is likely that some form of texture analysis could distinguish spurious regions better than the simple area filter performed currently. If sufficient numbers of regions were identified and labeled, neural networks could potentially be a useful tool for quantification and false positive rejection.

6.2.3 Microsphere transport and trapping model

While the microsphere transport model that both considered diameters and did not model embolic effects produced the most realistic cluster distributions of the ones considered, there were still significant differences between the true and simulated cluster distributions. For example, there were too many small clusters and too few large clusters. There are several potential improvements, described below, that could produce a more realistic distribution of cluster sizes.

One is the assumption that the probability of a microsphere entering the straighter child vessel for equal blood is 60%. While the dependence of particle traversal on both geometry and flow is well supported in the literature, the specific branching probability of 60% was taken from a fluid dynamics simulation that considered only two vessel generations in a single spatial arrangement. The branching probability of other vessel arrangements has not be reported, but it likely varies depending on both the relative angles and vessel blood flow in a more complicated manner than was used in this work. The large number of vessels in a full tree likely makes full fluid dynamics simulations computationally intractable, but it may be possible to perform simplified, but still more accurate, simulations of microsphere traversal at different junctions within the tree to produce unique branching probabilities for each type of junction.

An alternative model of particle infusion that used parameters to guide microsphere traversal was described by Högberg *et al*. This was specifically developed to produce cluster distributions more similar to resin microsphere cluster distributions. While the parameters they used to guide microsphere transport were not physically based, the physical parameters used in this work for tree growth and particle transport could be adapted to produce similar effects, though likely at the cost of some physical realism.

A more realistic model of particle infusion could simulate the concurrent traversal of a bolus of microspheres within the hepatic arterial tree. The presence of multiple spheres in a vessel as blood flow in the vessel decreases or stops due to embolic effects could produce different microsphere distributions than were observed with the models investigated in this work. This could potentially yield more large clusters like those observed in the porcine liver sample.

Comparisons between the micro-scale dose distributions observed in the porcine liver and the infusion simulations will also provide insight into how much of an impact different cluster distributions have on the probability of normal tissue toxicity. That would give a better understanding of the level of accuracy necessary for distribution simulation to be useful.

With more detailed and personalized models of the hepatic arterial tree, and with accurate simulations of microsphere trapping, it should be possible to accurately predict the dose distribution in both normal and tumor tissue. Micro-CT examination of tissue samples could also yield improvements to radiobiological models describing the survival of normal liver tissue in RE. Combining both improved models of microsphere distribution and RE impact could provide a dramatic improvement in the efficacy of RE treatments and both improve patient quality of life and allow a greater number of patients to receive curative treatments.

Bibliography

[1] R. L. Siegel, K. D. Miller, and A. Jemal, "Cancer statistics, 2017," *CA: a cancer journal for clinicians*, vol. 67, no. 1, pp. 7–30, 2017.

[2] J.-Q. Hu, F. Deng, X.-P. Hu, W. Zhang, X.-C. Zeng, and X.-F. Tian, "Histone deacetylase sirt6 regulates chemosensitivity in liver cancer cells via modulation of foxo3 activity," *Oncology reports*, vol. 40, no. 6, pp. 3635–3644, 2018.

[3] A. X. Zhu, D. G. Duda, D. V. Sahani, and R. K. Jain, "Hcc and angiogenesis: possible targets and future directions," *Nature reviews Clinical oncology*, vol. 8, no. 5, p. 292, 2011.

[4] S. Mittal and H. B. El-Serag, "Epidemiology of hcc: consider the population," *Journal of clinical gastroenterology*, vol. 47, p. S2, 2013.

[5] B. Blechacz and L. Mishra, "Hepatocellular carcinoma biology," in *Multidisciplinary Treatment of Hepatocellular Carcinoma*. Springer, 2013, pp. 1–20.

[6] J. de Ridder, J. H. de Wilt, F. Simmer, L. Overbeek, V. Lemmens, and I. Nagtegaal, "Incidence and origin of histologically confirmed liver metastases: an explorative case-study of 23,154 patients," *Oncotarget*, vol. 7, no. 34, p. 55368, 2016.

[7] K. Memon, R. J. Lewandowski, A. Riaz, and R. Salem, "Yttrium 90 microspheres for the treatment of hepatocellular carcinoma," in *Multidisciplinary Treatment of Hepatocellular Carcinoma*. Springer, 2013, pp. 207–224.

[8] A. S. Pasciak, A. C. Bourgeois, and Y. C. Bradley, "A microdosimetric analysis of absorbed dose to tumor as a function of number of microspheres per unit volume in 90y radioembolization," *Journal of Nuclear Medicine*, vol. 57, no. 7, pp. 1020–1026, 2016.

[9] A. K. Tong, Y. H. Kao, C. W. Too, K. F. Chin, D. C. Ng, and P. K. Chow, "Yttrium-90 hepatic radioembolization: clinical review and current techniques in interventional radiology and personalized dosimetry," *The British journal of radiology*, vol. 89, no. 1062, p. 20150943, 2016.

[10] S. Walrand, M. Hesse, C. Chiesa, R. Lhommel, and F. Jamar, "The low hepatic toxicity per gray of 90y glass microspheres is linked to their transport in the arterial tree favoring a nonuniform trapping as observed in post-therapy pet imaging," *J Nucl Med*, vol. 55, no. 1, pp. 135–140, 2014.

[11] S. Walrand, M. Hesse, F. Jamar, and R. Lhommel, “A hepatic dose-toxicity model opening the way toward individualized radioembolization planning,” *J Nucl Med*, vol. 55, no. 8, pp. 1317–22, 2014.

[12] M. Cremonesi, C. Chiesa, L. Strigari, M. Ferrari, F. Botta, F. Guerriero, C. De Cicco, G. Bonomo, F. Orsi, L. Bodei *et al.*, “Radioembolization of hepatic lesions from a radiobiology and dosimetric perspective,” *Frontiers in oncology*, vol. 4, p. 210, 2014.

[13] C. Chiesa, K. S. Gleisner, G. Flux, J. Gear, S. Walrand, K. Bacher, U. Eberlein, E. Visser, N. Chouin, M. Ljungberg *et al.*, “The conflict between treatment optimization and registration of radiopharmaceuticals with fixed activity posology in oncological nuclear medicine therapy,” 2017.

[14] S. Gnesin, L. Canetti, S. Adib, N. Cherbuin, M. S. Monteiro, P. Bize, A. Denys, J. O. Prior, S. Baechler, and A. Boubaker, “Partition model–based 99mtc-maa spect/ct predictive dosimetry compared with 90y tof pet/ct posttreatment dosimetry in radioembolization of hepatocellular carcinoma: A quantitative agreement comparison,” *Journal of Nuclear Medicine*, vol. 57, no. 11, pp. 1672–1678, 2016.

[15] J. Högberg, M. Rizell, R. Hultborn, J. Svensson, O. Henrikson, J. Mölne, P. Gjertsson, and P. Bernhardt, “Simulation model of microsphere distribution for selective internal radiation therapy agrees with observations,”

International Journal of Radiation Oncology Biology* Physics*, vol. 96, no. 2, pp. 414–421, 2016.

[16] K. Van de Graaff, R. W. Rhees, and S. L. Palmer, *Schaum's Outline of Human Anatomy and Physiology: 1,440 Solved Problems+ 20 Videos*. McGraw-Hill Professional, 2013.

[17] W. W. Lautt, “Hepatic circulation: physiology and pathophysiology,” in *Colloquium Series on Integrated Systems Physiology: from Molecule to Function*, vol. 1, no. 1. Morgan & Claypool Publishers, 2009, pp. 1–174.

[18] B. Vollmar and M. D. Menger, “The hepatic microcirculation: mechanistic contributions and therapeutic targets in liver injury and repair,” *Physiological reviews*, vol. 89, no. 4, pp. 1269–1339, 2009.

[19] W. A. Dezarn, J. T. Cessna, L. A. DeWerd, W. Feng, V. L. Gates, J. Halama, A. S. Kennedy, S. Nag, M. Sarfaraz, V. Sehgal *et al.*, “Recommendations of the american association of physicists in medicine on dosimetry, imaging, and quality assurance procedures for 90y microsphere brachytherapy in the treatment of hepatic malignancies,” *Medical physics*, vol. 38, no. 8, pp. 4824–4845, 2011.

[20] G. Noussios, I. Dimitriou, I. Chatzis, and A. Katsourakis, “The main anatomic variations of the hepatic artery and their importance in surgical

practice: review of the literature," *Journal of clinical medicine research*, vol. 9, no. 4, p. 248, 2017.

[21] A. R. Crawford, X.-Z. Lin, and J. M. Crawford, "The normal adult human liver biopsy: a quantitative reference standard," *Hepatology*, vol. 28, no. 2, pp. 323–331, 1998.

[22] Z. Kan and D. C. Madoff, "Liver anatomy: microcirculation of the liver," in *Seminars in interventional radiology*, vol. 25, no. 2. Thieme Medical Publishers, 2008, p. 77.

[23] N. Nagasue, H. Yukaya, Y. Ogawa, H. Kohno, and T. Nakamura, "Human liver regeneration after major hepatic resection. a study of normal liver and livers with chronic hepatitis and cirrhosis." *Annals of surgery*, vol. 206, no. 1, p. 30, 1987.

[24] J. Bruix and M. Sherman, "Management of hepatocellular carcinoma," *Hepatology*, vol. 42, no. 5, pp. 1208–1236, 2005.

[25] E. A. Tsochatzis, G. Germani, and A. K. Burroughs, "Transarterial chemoembolization, transarterial chemotherapy, and intra-arterial chemotherapy for hepatocellular carcinoma treatment," in *Seminars in oncology*, vol. 37, no. 2. Elsevier, 2010, pp. 89–93.

[26] B. Sangro, M. Iñarrairaegui, and J. I. Bilbao, "Radioembolization for hep-

atocellular carcinoma," *Journal of hepatology*, vol. 56, no. 2, pp. 464–473, 2012.

[27] J. L. Prince and J. M. Links, *Medical imaging signals and systems*. Pearson Prentice Hall Upper Saddle River, NJ, 2006.

[28] S. R. Cherry, J. Sorenson, M. E. Phelps, and B. M. Methé, "Physics in nuclear medicine," *Medical Physics*, vol. 31, no. 8, pp. 2370–2371, 2004.

[29] G. Sgouros and R. F. Hobbs, "Dosimetry for radiopharmaceutical therapy," in *Seminars in nuclear medicine*, vol. 44, no. 3. Elsevier, 2014, pp. 172–178.

[30] S. A. Gulec, M. L. Sztejnberg, J. A. Siegel, T. Jevremovic, and M. Stabin, "Hepatic structural dosimetry in 90y microsphere treatment: a monte carlo modeling approach based on lobular microanatomy," *Journal of Nuclear Medicine*, vol. 51, no. 2, p. 301, 2010.

[31] G. Sgouros and R. F. Hobbs, "Patient-specific dosimetry, radiobiology, and the previously-treated patient," in *Therapeutic Nuclear Medicine*. Springer, 2012, pp. 737–745.

[32] R. Baskar, J. Dai, N. Wenlong, R. Yeo, and K.-W. Yeoh, "Biological response of cancer cells to radiation treatment," *Frontiers in molecular biosciences*, vol. 1, p. 24, 2014.

[33] W. E. Bolch, K. F. Eckerman, G. Sgouros, and S. R. Thomas, “Mird pamphlet no. 21: a generalized schema for radiopharmaceutical dosimetry–standardization of nomenclature,” *Journal of Nuclear Medicine*, vol. 50, no. 3, p. 477, 2009.

[34] E. Garin, Y. Rolland, M. Pracht, S. Le Sourd, S. Laffont, H. Mesbah, L.-A. Haumont, L. Lenoir, T. Rohou, V. Brun *et al.*, “High impact of macroaggregated albumin-based tumour dose on response and overall survival in hepatocellular carcinoma patients treated with 90y-loaded glass microsphere radioembolization,” *Liver International*, vol. 37, no. 1, pp. 101–110, 2017.

[35] P. Haste, M. Tann, S. Persohn, T. LaRoche, V. Aaron, T. Mauxion, N. Chauhan, M. R. Dreher, and M. S. Johnson, “Correlation of technetium-99m macroaggregated albumin and yttrium-90 glass microsphere biodistribution in hepatocellular carcinoma: A retrospective review of pretreatment single photon emission ct and posttreatment positron emission tomography/ct,” *Journal of Vascular and Interventional Radiology*, vol. 28, no. 5, pp. 722–730, 2017.

[36] M. Wondergem, M. Smits, M. Elschot, H. de Jong, H. M. Verkooijen, M. van den Bosch, J. Nijsen, and M. Lam, “99mtc-macroaggregated albumin poorly predicts the intrahepatic distribution of 90y resin micro-

spheres in hepatic radioembolization," *J Nucl Med*, vol. 54, no. 8, pp. 1294–301, 2013.

[37] L. A. Dawson, R. K. Ten Haken, and T. S. Lawrence, "Partial irradiation of the liver," in *Seminars in radiation oncology*, vol. 11, no. 3. Elsevier, 2001, pp. 240–246.

[38] Y. Kuwahara, M. Mori, S. Kitahara, M. Fukumoto, T. Ezaki, S. Mori, S. Echigo, Y. Ohkubo, and M. Fukumoto, "Targeting of tumor endothelial cells combining 2 gy/day of x-ray with everolimus is the effective modality for overcoming clinically relevant radioresistant tumors," *Cancer medicine*, vol. 3, no. 2, pp. 310–321, 2014.

[39] M. Abdelfattah, M. Al-Sebayel, D. Broering, and H. Alsuhaibani, "Radioembolization using yttrium-90 microspheres as bridging and downstaging treatment for unresectable hepatocellular carcinoma before liver transplantation: initial single-center experience," in *Transplantation proceedings*, vol. 47, no. 2. Elsevier, 2015, pp. 408–411.

[40] K. Bryce and E. A. Tsochatzis, "Downstaging for hepatocellular cancer: harm or benefit?" *Translational gastroenterology and hepatology*, vol. 2, 2017.

[41] M. Iñarrairaegui, F. Pardo, J. Bilbao, F. Rotellar, A. Benito, D. D'Avola, J. Herrero, M. Rodriguez, P. Martí, G. Zozaya *et al.*, "Response to ra-

dioembolization with yttrium-90 resin microspheres may allow surgical treatment with curative intent and prolonged survival in previously unresectable hepatocellular carcinoma," *European Journal of Surgical Oncology (EJSO)*, vol. 38, no. 7, pp. 594–601, 2012.

[42] S. Sternberg, *Histology for pathologists*. Raven Press, 1992. [Online]. Available: https://books.google.com/books?id=TstpAAAAMAAJ

[43] A. M. Campbell, I. H. Bailey, and M. A. Burton, "Analysis of the distribution of intra-arterial microspheres in human liver following hepatic yttrium-90 microsphere therapy," *Physics in Medicine & Biology*, vol. 45, no. 4, p. 1023, 2000.

[44] F. E. Zink, "X-ray tubes." *Radiographics*, vol. 17, no. 5, pp. 1259–1268, 1997.

[45] G. L. Zeng, "Revisit of the ramp filter," in *2014 IEEE Nuclear Science Symposium and Medical Imaging Conference (NSS/MIC)*. IEEE, 2014, pp. 1–6.

[46] B. D. Metscher, "Microct for developmental biology: A versatile tool for high-contrast 3d imaging at histological resolutions," *Developmental dynamics: an official publication of the American Association of Anatomists*, vol. 238, no. 3, pp. 632–640, 2009.

[47] M. Marxen, C. Paget, L. Yu, and R. Henkelman, “Estimating perfusion using microct to locate microspheres,” *Physics in Medicine & Biology*, vol. 51, no. 1, p. N9, 2005.

[48] a. B. I. g. c. Biocompatibles UK Ltd., *Therasphere USA Package Insert Rev. 14*, 2004 (accessed December 19, 2017), https://www.btg-im.com/BTG/media/TheraSphere-Documents/PDF/TheraSphere-Package-Insert_USA_Rev-14.pdf.

[49] J. Bézy-Wendling and A. Bruno, “A 3d dynamic model of vascular trees,” *Journal of Biological Systems*, vol. 7, no. 01, pp. 11–31, 1999.

[50] M. Kretowski, Y. Rolland, J. Bézy-Wendling, and J.-L. Coatrieux, “Physiologically based modeling of 3-d vascular networks and ct scan angiography,” *IEEE transactions on medical imaging*, vol. 22, no. 2, pp. 248–257, 2003.

[51] J. Högberg, M. Rizell, R. Hultborn, J. Svensson, O. Henrikson, J. Mölne, P. Gjertsson, and P. Bernhardt, “Increased absorbed liver dose in selective internal radiation therapy (sirt) correlates with increased sphere-cluster frequency and absorbed dose inhomogeneity,” *EJNMMI physics*, vol. 2, no. 1, p. 10, 2015.

[52] R. Revellin, F. Rousset, D. Baud, and J. Bonjour, “Extension of murray’s

law using a non-newtonian model of blood flow," *Theoretical Biology and Medical Modelling*, vol. 6, no. 1, p. 7, 2009.

[53] R. S. Reneman and A. P. Hoeks, "Wall shear stress as measured in vivo: consequences for the design of the arterial system," *Medical & biological engineering & computing*, vol. 46, no. 5, pp. 499–507, 2008.

[54] L. A. d. Silveira, F. B. C. Silveira, and V. P. S. Fazan, "Arterial diameter of the celiac trunk and its branches: anatomical study," *Acta cirurgica brasileira*, vol. 24, no. 1, pp. 43–47, 2009.

[55] A. Pries, D. Neuhaus, and P. Gaehtgens, "Blood viscosity in tube flow: dependence on diameter and hematocrit," *American Journal of Physiology-Heart and Circulatory Physiology*, vol. 263, no. 6, pp. H1770–H1778, 1992.

[56] G. Lowe, "1 blood rheology in vitro and in vivo," *Bailliere's clinical haematology*, vol. 1, no. 3, pp. 597–636, 1987.

[57] C. Eipel, K. Abshagen, and B. Vollmar, "Regulation of hepatic blood flow: the hepatic arterial buffer response revisited," *World journal of gastroenterology: WJG*, vol. 16, no. 48, p. 6046, 2010.

[58] G. Mancia, A. Ferrari, L. Gregorini, G. Parati, G. Pomidossi, G. Bertinieri, G. Grassi, M. di Rienzo, A. Pedotti, and A. Zanchetti, "Blood pressure and

heart rate variabilities in normotensive and hypertensive human beings." *Circulation research*, vol. 53, no. 1, pp. 96–104, 1983.

[59] M. Kretowski, Y. Rolland, J. Bézy-Wendling, and J.-L. Coatrieux, "Fast algorithm for 3-d vascular tree modeling," *Computer methods and programs in biomedicine*, vol. 70, no. 2, pp. 129–136, 2003.

[60] W. Segars, G. Sturgeon, S. Mendonca, J. Grimes, and B. M. Tsui, "4d xcat phantom for multimodality imaging research," *Medical physics*, vol. 37, no. 9, pp. 4902–4915, 2010.

[61] S. Srihari, "Representation of three-dimensional digital images," *ACM Computing Surveys (CSUR)*, vol. 13, no. 4, pp. 399–424, 1981.

[62] M. Zamir, "Optimality principles in arterial branching," *Journal of Theoretical Biology*, vol. 62, no. 1, pp. 227–251, 1976.

[63] W. Schreiner, F. Neumann, M. Neumann, A. End, S. M. Roedler, and S. Aharinejad, "The influence of optimization target selection on the structure of arterial tree models generated by constrained constructive optimization." *The Journal of general physiology*, vol. 106, no. 4, pp. 583–599, 1995.

[64] G. S. Fung, W. P. Segars, G. T. Gullberg, and B. M. Tsui, "Development of

a model of the coronary arterial tree for the 4d xcat phantom," *Physics in Medicine & Biology*, vol. 56, no. 17, p. 5651, 2011.

[65] T. Arts, R. Kruger, W. Van Gerven, J. Lambregts, and R. Reneman, "Propagation velocity and reflection of pressure waves in the canine coronary artery," *American Journal of Physiology-Heart and Circulatory Physiology*, vol. 237, no. 4, pp. H469–H474, 1979.

[66] K. Carlisle, M. Halliwell, A. Read, and P. Wells, "Estimation of total hepatic blood flow by duplex ultrasound." *Gut*, vol. 33, no. 1, pp. 92–97, 1992.

[67] K. M. Pillai, P. E. McKeever, C. A. Knutsen, P. A. Terrio, D. M. Prieskorn, and W. D. Ensminger, "Microscopic analysis of arterial microsphere distribution in rabbit liver and hepatic vx2 tumor," *Selective cancer therapeutics*, vol. 7, no. 2, pp. 39–48, 1991.

[68] N. R. Crookston, G. S. Fung, and E. C. Frey, "Development of a customizable hepatic arterial tree and particle transport model for use in treatment planning," *IEEE Transactions on Radiation and Plasma Medical Sciences*, vol. 3, no. 1, pp. 31–37, 2019.

[69] A. S. Kennedy, C. Nutting, D. Coldwell, J. Gaiser, and C. Drachenberg, "Pathologic response and microdosimetry of 90y microspheres in man: review of four explanted whole livers," *International Journal of Radiation Oncology* Biology* Physics*, vol. 60, no. 5, pp. 1552–1563, 2004.

[70] J. Högberg, M. Rizell, R. Hultborn, J. Svensson, O. Henrikson, J. Mölne, P. Gjertsson, and P. Bernhardt, "Heterogeneity of microsphere distribution in resected liver and tumour tissue following selective intrahepatic radiotherapy," *EJNMMI research*, vol. 4, no. 1, p. 48, 2014.

[71] P. Roberson, R. H. Ten, D. McShan, P. McKeever, and W. Ensminger, "Three-dimensional tumor dosimetry for hepatic yttrium-90-microsphere therapy." *Journal of nuclear medicine: official publication, Society of Nuclear Medicine*, vol. 33, no. 5, pp. 735–738, 1992.

[72] R. Fox, P. Klemp, G. Egan, L. Mina, M. Burton, and B. Gray, "Dose distribution following selective internal radiation therapy," *International Journal of Radiation Oncology* Biology* Physics*, vol. 21, no. 2, pp. 463–467, 1991.

[73] L. Najman and H. Talbot, *Mathematical morphology: from theory to applications*. John Wiley & Sons, 2013.

[74] R. C. Gonzalez, R. E. Woods, S. L. Eddins *et al.*, "Digital image processing using matlab. 2004," *Publisher T. Robbins, Printed in USA*, vol. 11, pp. 531–534, 2009.

[75] C. J. Werner, J. S. Bull, C. J. Solomon, F. B. Brown, G. W. McKinney, M. E. Rising, D. A. Dixon, R. L. Martz, H. G. Hughes, L. J. Cox *et al.*, "Mcnp

version 6.2 release notes," Los Alamos National Lab.(LANL), Los Alamos, NM (United States), Tech. Rep., 2018.

[76] K. Eckerman, R. Westfall, J. Ryman, and M. Cristy, "Availability of nuclear decay data in electronic form, including beta spectra not previously published." *Health physics*, vol. 67, no. 4, pp. 338–345, 1994.

[77] I. C. on Radiation Units and Measurements, "Photon, electron, proton and neutron interaction data for body tissues," *ICRU Report No. 46*, 1992.

[78] A. Riaz, L. Kulik, R. J. Lewandowski, R. K. Ryu, G. G. Spear, M. F. Mulcahy, M. Abecassis, T. Baker, V. Gates, R. Nayar *et al.*, "Radiologic–pathologic correlation of hepatocellular carcinoma treated with internal radiation using yttrium-90 microspheres," *Hepatology*, vol. 49, no. 4, pp. 1185–1193, 2009.

[79] K. P. Willowson, M. Tapner, D. L. Bailey *et al.*, "A multicentre comparison of quantitative 90 y pet/ct for dosimetric purposes after radioembolization with resin microspheres," *European journal of nuclear medicine and molecular imaging*, vol. 42, no. 8, pp. 1202–1222, 2015.

[80] A. Nykonenko, P. Vavra, and P. Zonča, "Anatomic peculiarities of pig and human liver." *Experimental and clinical transplantation: official journal of the Middle East Society for Organ Transplantation*, vol. 15, no. 1, pp. 21–26, 2017.

Curriculum Vitae

Nathan Crookston (b. 1982) was raised in Kaysville, Utah, USA.

Nathan received a Bachelor of Science in Electrical Engineering with minors in Computer Science and Mathematics in December of 2006 from Utah State University in Logan, Utah. Following graduation, Nathan worked as a Software Engineer working on tactical image visualization at Space Dynamics Laboratory for 8 years. He also earned a Master of Science in Computer Engineering in 2012 under the guidance of Brandon Eames and Jake Gunther, where he created a project to prototype and visualize the outputs of synthetic aperture radar algorithms.

In 2014, Nathan began his studies at Johns Hopkins University. In that time he served as a teaching assistant for Image Processing I and II for three semesters. He received awards for “best student paper in dosimetry applications” and “overall best student paper” at the 6th International Workshop on Computational Human Phantoms in 2017.